



**HAL**  
open science

## Acoustic and mechanical properties of Nankai accretionary prism core samples

Hugues Raimbourg, Yozo Hamano, Saneatsu Saito, Masataka Kinoshita,  
Achim Kopf

► **To cite this version:**

Hugues Raimbourg, Yozo Hamano, Saneatsu Saito, Masataka Kinoshita, Achim Kopf. Acoustic and mechanical properties of Nankai accretionary prism core samples. *Geochemistry, Geophysics, Geosystems*, 2011, 12 (4), pp.1-28. 10.1029/2010GC003169 . insu-00627809

**HAL Id: insu-00627809**

**<https://insu.hal.science/insu-00627809>**

Submitted on 29 Sep 2011

**HAL** is a multi-disciplinary open access archive for the deposit and dissemination of scientific research documents, whether they are published or not. The documents may come from teaching and research institutions in France or abroad, or from public or private research centers.

L'archive ouverte pluridisciplinaire **HAL**, est destinée au dépôt et à la diffusion de documents scientifiques de niveau recherche, publiés ou non, émanant des établissements d'enseignement et de recherche français ou étrangers, des laboratoires publics ou privés.



## Acoustic and mechanical properties of Nankai accretionary prism core samples

**Hugues Raimbourg**

*JAMSTEC, Natsushima-cho, Yokosuka 237-0061, Japan*

*Now at Institut des Sciences de la Terre d'Orléans, Université d'Orléans, 1a rue de la Férollerie, F-45071 Orléans, France (hugues.raimbours@univ-orleans.fr)*

**Yozo Hamano, Saneatsu Saito, and Masataka Kinoshita**

*JAMSTEC, Natsushima-cho, Yokosuka 237-0061, Japan*

**Achim Kopf**

*MARUM, University of Bremen, PO Box 330440, D-28334 Bremen, Germany*

[1] We studied undeformed sediment and accreted strata recently recovered by Ocean Drilling Program/Integrated Ocean Drilling Program (ODP/IODP) drilling in Nankai Trough convergent margin to unravel the changes in physical properties from initial deposition to incipient deformation. We have derived acoustic ( $V_p$ ) and mechanical (uniaxial poroelastic compliance, compaction amplitude) properties of samples from various drill sites along the Muroto (ODP 1173) and Kii transects (IODP C0001, C0002, C0006, and C0007) from isotropic loading tests where confining and pore pressure were independently applied. We quantified the dependence of  $V_p$  on both effective ( $P_{\text{eff}}$ ) and confining ( $P_c$ ) pressure, which can be used to correct atmospheric pressure measurements of  $V_p$ . Experimental  $V_p$  obtained on core samples extrapolated to in situ conditions are slightly higher than logging-derived velocities, which can be attributed either to velocity dispersion or to the effect of large-scale faults and weak zones on waves with longer wavelength. In the high-porosity (30%–60%) tested sediments, velocities are controlled at first order by porosity and not by lithology, which is in agreement with our static measurements of drained framework incompressibility, much smaller than fluid incompressibility. Rather than framework incompressibility, shear modulus is probably the second-order control on  $V_p$ , accounting for most of the difference between actual  $V_p$  and the prediction by Wood's (1941) suspension model. We also quantified the mechanical state of Nankai samples in terms of anisotropy, diagenesis, and consolidation. Both acoustic and mechanical parameters reveal similar values in vertical and horizontal directions, attesting to the very low anisotropy of the tested material. When considering the porous samples of the Upper Shikoku Basin sediments (Site 1173) as examples of diagenetically cemented material, several mechanical and acoustic attributes appeared as reliable experimental indicators of the presence of intergrain cementation. We also detected incipient cementation in samples from IODP Site C0001 (accretionary prism unit). In terms of consolidation, we distinguished two classes of material response (shallow, deformable samples and deep, hardly deformable ones) based on the amount of compaction upon application of a  $P_{\text{eff}}$  large with respect to the inferred in situ value, with a transition that might be related to a critical porosity.

**Components:** 15,300 words, 15 figures, 1 table.

**Keywords:** mechanical properties;  $P$  wave velocity; Nankai; compaction; experiments.

**Index Terms:** 3036 Marine Geology and Geophysics: Ocean drilling; 3060 Marine Geology and Geophysics: Subduction zone processes (1031, 3613, 8170, 8413); 5102 Physical Properties of Rocks: Acoustic properties.



**Received** 14 April 2010; **Revised** 20 January 2011; **Accepted** 27 January 2011; **Published** 7 April 2011.

Raimbourg, H., Y. Hamano, S. Saito, M. Kinoshita, and A. Kopf (2011), Acoustic and mechanical properties of Nankai accretionary prism core samples, *Geochem. Geophys. Geosyst.*, 12, Q0AD10, doi:10.1029/2010GC003169.

**Theme:** Mechanics, Deformation, and Hydrologic Processes at Subduction Complexes,  
With Emphasis on the Nankai Trough Seismogenic Zone Experiment  
(NanTroSEIZE) Drilling Transect  
**Guest Editors:** D. Saffer, P. Henry, and H. Tobin

## 1. Introduction

[2] In accretionary prisms such as Nankai, overpressures, i.e., pore fluid pressures exceeding hydrostatic values, within the décollement have been paid much attention as they provide an efficient way to reduce the friction and have a large impact on seismic rupture around the updip limit of the seismogenic zone [Bangs *et al.*, 2009; Moore *et al.*, 1995; Tobin and Saffer, 2009]. Unfortunately, direct measurement of pore fluid pressure is difficult to achieve and overpressures are often inferred indirectly, for example from a low Poisson's ratio estimated using seismic velocities  $V_p$  and  $V_s$  [Dvorkin *et al.*, 1999a], or through the large-scale modeling of prism fluid circulation [Saffer and Bekins, 1998, 2006].

[3] Another method consists in converting seismic velocity into porosity to estimate the state of compaction and to infer possible overpressures [e.g., Tobin and Saffer, 2009]. The  $V_p$  porosity relationships are experimentally calibrated with well logs or cm-thick discrete core samples [Erickson and Jarrard, 1998; Hoffman and Tobin, 2004; Hyndman *et al.*, 1993], while the velocities on which such laws are applied are determined during seismic reflection campaigns, i.e., with a resolution of tens of meters at best. In addition to this problem of wave frequency, another problem is restoring velocities measured on core at atmospheric pressure to in situ conditions. Hamilton [1971a] proposed corrections for subseafloor sediments, but the problem remains for deeper samples.

[4] More generally, the interpretation of geophysical profiles of  $V_p$  [e.g., Tobin and Saffer, 2009] or seismic impedance [Bangs *et al.*, 1999; Bangs and Gulick, 2005; Park *et al.*, 2002] rely on the knowledge of the evolution of the material during burial, in particular its consolidation, i.e., the reduction in porosity as a result of overburden increase. Although simple compaction curves [Athy, 1930] assume a very simple relationship

between depth and porosity, actual consolidation is much more complex and porosity profiles are often ambiguous as they reflect hydrological state and possible overpressures [Screaton *et al.*, 2002] as well as the internal strength of the rocks, which depends on lithology and diagenesis [Morgan and Ask, 2004]. In this respect, the experimental analysis of material strength evolution during consolidation is key to interpreting geophysical data.

[5] In this paper we present the results of mechanical, isotropic experiments carried out on samples collected in the Nankai subduction zone during ODP Leg 190 (Site 1173) and IODP Legs 315/316 (Sites C0001, C0002, C0006, C0007) to characterize their mechanical (poroelastic, plastic) and acoustic properties. The first objective of this experimental study is to provide experimental constraints on simple theoretical poroelastic models of high-porosity (30%–60%) sediments, in order (1) to derive correction factors to restore to in situ conditions velocities measured at atmospheric pressure on discrete core samples (i.e., the standard IODP laboratory routine) and (2) to interpret the relationship between  $V_p$  and porosity. Core-scale, experimental  $V_p$  are also compared to logging/seismic data for integration of velocity data sets. The second objective of our tests is to further characterize the mechanical state of shallow ( $\leq 1000$  mbsf) samples from the Nankai Trough area, which includes estimation of anisotropy, distribution of rock-strengthening cement/thermal alteration and response to experimental consolidation. Finally, we discuss the relevance of the concept of critical porosity in the light of our experimental results.

## 2. Tectonic Setting

[6] The continuous convergence of Philippine Sea and Eurasian plates in Japan is responsible for the growth of a large accretionary prism since the Cretaceous [Taira *et al.*, 1988], whose active por-

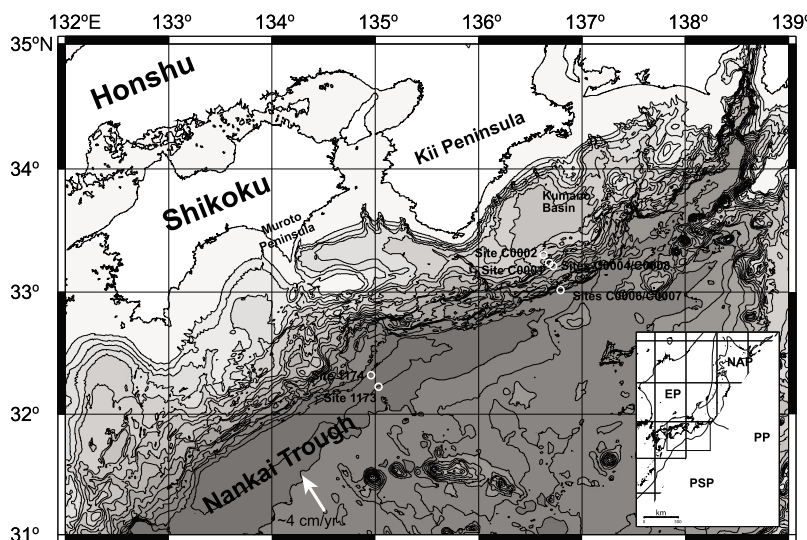


**Figure 1.** Map of the Nankai Trough, including the Kumano and Muroto transects investigated during ODP Legs 190/196 and IODP Legs 314/315/316 [Moore *et al.*, 2009].

tion, the Nankai Trough accretionary prism, is submarine and extends on several hundred kilometers along strike near the southwestern margin of Japan. Successive drilling within the Deep Sea Drilling Program (DSDP Legs 31, 87), the Ocean Drilling Program (ODP Legs 131, 190, 196) and NanTroSEIZE (Nankai Trough Seismogenic Zone Experiment) expeditions of Integrated Ocean Drilling Program (IODP Legs 314, 315, 316, 319, 322) and seismic reflection campaigns [Moore *et al.*, 2005; *Shipboard Scientific Party*, 1991a; Tobin *et al.*, 2009a] enabled to determine the internal structure of the wedge as decomposed into an outer section with a steep slope and active folding and thrusting and an inner section, more gently inclined and overlain by a fore-arc basin (i.e., the Kumano Basin).

[7] Although the internal structure of the prism varies slightly laterally between transects off Muroto Peninsula (ODP Leg 190) and Kii Peninsula (IODP Legs 314/315/316) (Figure 1), in both settings it can be roughly divided into equivalent tectonostratigraphic units, from which we collected samples for testing (site location between brackets). Incoming sediments, located seaward of the prism, are composed of a lower sequence of hemipelagic sediments of the Shikoku Basin (ODP Site 1173), overlain by a variable thickness of trench turbidites. The wedge is made of frontally accreted and deformed sediments, composed of either hemipelagic material or trench turbidites (IODP Sites C0001, C0006, C0007), overlain by slope sediments and underlain by underthrust sediments. The fore-arc basin is

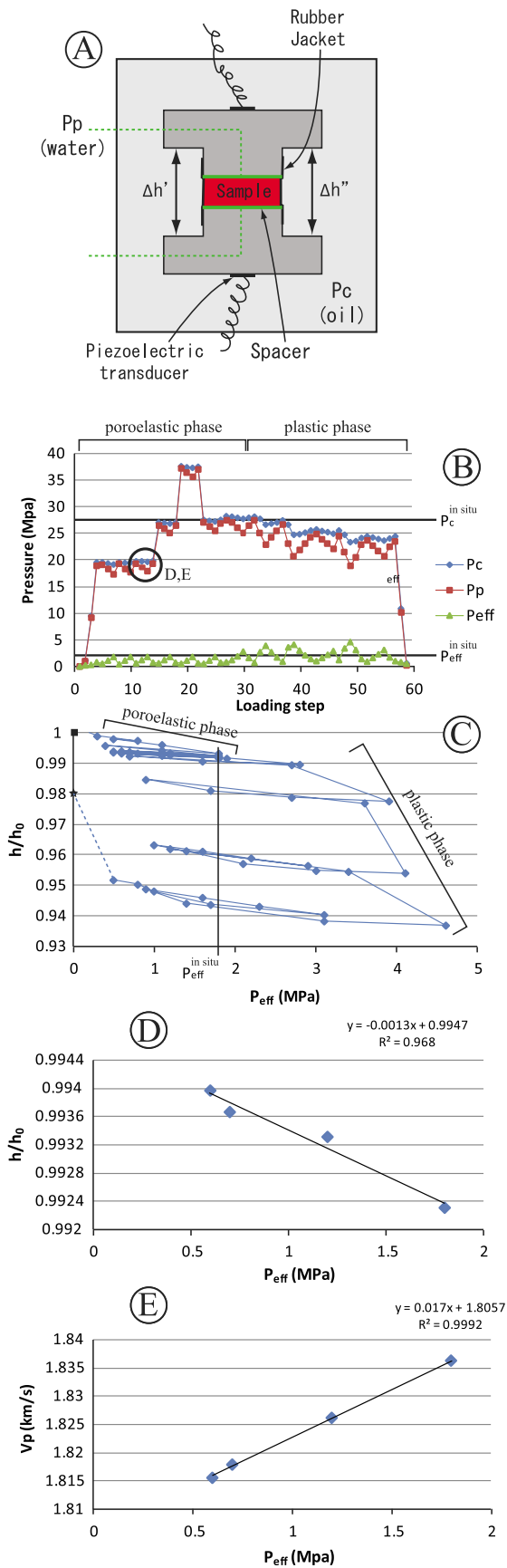
composed of thick, turbiditic material deposited over the inner wedge (IODP Site C0002).

### 3. Experimental Procedure

#### 3.1. Principle

[8] Tested samples are cylinders with 1.5 in. ( $\approx 3.8$  cm) diameter and 10–20 mm height, cut by a diamond saw from ODP/IODP cores (Figure 2). Experiments were carried out within an oil high-pressure vessel, where  $P_c$ , the confining pressure is fixed, while two independent water lines enable us to control  $P_p$ , the pore fluid pressure on both circular faces of the cylinder (the continuity of the fluid film from the pipes to the flat surface of the sample is ensured by the placement of metal filters on sample surfaces). For each set ( $P_c$ ,  $P_p$ ) of applied conditions, we measured sample height variations from two diametrically located points ( $\Delta h = \frac{\Delta h_1 + \Delta h_2}{2}$ ) as well as the time necessary for a compressional wave to propagate through the sample.

[9] Experiments described here differ from usual consolidation experiments [Johns, 1986; Karig and Ask, 2003; Saffer, 2003] where uniaxial, vertical loading aims at reproducing in situ conditions prevailing during compaction. Our experiments were not meant to simulate in situ loading, but to assess the mechanical and acoustic state of the specimen using variable conditions of isotropic confining and pore pressures in an instrumented autoclave vessel.



### 3.2. Experimental Devices and Precision

[10] Sample height variations  $\Delta h$  are measured by two Linear Variable Differential Transformers (LVDT), with a precision of  $\sim 1 \mu m$ , which measure the displacement between the 2 holders on either side of the sample. The precision on sample *absolute* height  $h = h_0 - \Delta h$  is in the order of  $\sim 100 \mu m$ , i.e., of much lower accuracy than the internal parameters, because (1) of possible movement of the holder during the insertion inside the high-pressure vessel and the first application of  $P_c$  and (2) the low precision on the sample initial height  $h_0$ , measured out of the chamber with a caliper. In contrast, the precision in *relative* height variations is comparable to LVDT accuracy.

[11] Compressional wave velocity  $V_p$  is measured using two piezoelectric transducers glued to the sample holder in titanium, which vibrate at a 3 MHz frequency. Travel time is estimated by hand picking of the wave arrival with a precision that depends on the signal quality, but that we estimate to be  $\sim 0.1 \mu s$ . The precision in relative travel time between two sets of conditions, estimated by the correlation between the two waveforms is much higher ( $\sim 0.01 \mu s$ ).

### 3.3. Mechanical Tests

[12] For each studied samples, the test was decomposed into the three phases described hereafter. For

**Figure 2.** (a) Experimental device of isotropic loading, where we measure variations in sample height  $\Delta h = \frac{\Delta h' + \Delta h''}{2}$  following  $P_c$  and  $P_p$  evolution. (b) Associated typical loading path, decomposed into a first, poroelastic phase, where  $P_{eff}$  is kept below  $P_{eff}^{in-situ}$  and poroelastic compliance  $\frac{1}{h_0} \frac{\partial h}{\partial P_{eff}}$  as well as  $V_p$  dependence on  $P_{eff}$  (i.e.,  $\frac{\partial V_p}{\partial P_{eff}}$ ) are estimated, and a second phase where the potential plastic deformation upon application of a large  $P_{eff}$  with respect to in situ conditions is assessed. (c) Associated normalized height evolution within the pressure vessel. Apart from an initial and limited decrease in height, partly due to filter shrinkage and holder movement, during the first phase of deformation, applied through cycles of  $P_{eff}$  for several  $P_c$  increments, deformation appears almost reversible. During the second phase, large shrinkage occurs and persists even upon  $P_{eff}$  release. Square (star) is the initial (final) normalized height measured out of the chamber. (d, e) Elementary step of poroelastic phase 1 (indicated in Figure 2c): for a given  $P_c$ , several  $P_{eff}$  are applied, enabling to derive the compliance  $\frac{1}{h_0} \frac{\partial h}{\partial P_{eff}}$  (Figure 2d) as well as  $\frac{\partial V_p}{\partial P_{eff}}$  (Figure 2e) (sample C0001H-5H-vert).



any samples, we defined in situ effective pressure  $P_{\text{eff}}^{\text{in-situ}}$  as

$$P_{\text{eff}}^{\text{in-situ}} = \sigma_v - \rho_f g z,$$

where  $\sigma_v$  is the load of the rock column overlying the tested sample  $z$ , its thickness, and  $\rho_f$  the fluid density. Note that this value is not the actual in situ effective pressure, as in most cases no direct measurement is available, but a theoretical value calculated for hydrostatic pore fluid pressure. Actual in situ pore fluid pressure is larger than hydrostatic value (for fluid expulsion and compaction to proceed), but we suppose that the difference is small, because all our samples are relatively shallow, with relatively high porosity/permeability and they have not been subjected to rapid loading like material underthrust below the decollement. Furthermore, Site 1173 is used as a reference site where excess pore pressure is considered as negligible [e.g., *Screaton et al.*, 2002] and direct measurements at depths in Kumano fore-arc basin confirm pore fluid close to hydrostatic conditions [*Saffer et al.*, 2009].

### 3.3.1. Initial Resaturation

[13] After insertion of the specimen into the high-pressure vessel, full rehydration and saturation prior to testing is ensured by raising the confining pressure  $P_c$  and pore fluid pressure  $P_p$  simultaneously to  $P_c \sim 1$  MPa and effective pressure  $P_{\text{eff}}$  of the order of a few tenths of MPa. Upon transmission of the pressure through the pores, two simultaneous phenomena contribute to resaturation; first, the gas initially present is mechanically compressed so that its volume is divided by a factor equal to the pore pressure (when expressed in bars) and second, increase in pressure triggers gas dissolution in the liquid.

[14] The applied effective pressure  $P_{\text{eff}}$  is fixed to a value well below the in situ effective pressure. The samples are left with these conditions overnight before the mechanical test starts. Height variations during this phase are limited to a few tens of microns, i.e., a few permil, which illustrates that the samples were already close to saturation in their initial state after coring and cool storage.

### 3.3.2. Poroelastic Phase

[15] Once the experiment has started, the first phase of loading consists in applying incrementally different magnitudes of  $P_{\text{eff}}$  (Figures 2b and 2c) while  $P_c$  is kept at a fixed value. We impose during this phase the effective pressure to be kept below  $P_{\text{eff}}^{\text{in-situ}}$ .

[16] Although  $V_p$  and height variations are not linear over a large  $P_{\text{eff}}$  range [e.g., *Tobin and Moore*, 1994], in the range 0.5–3 MPa for deep samples (ca. > 300 mbsf) and 0.5– $P_{\text{eff}}^{\text{in-situ}}$  for shallow samples (<300 mbsf), our samples can be reasonably considered as linear (e.g., Figures 2d and 2e). We can thus use height variations to derive a poroelastic coefficient equivalent to a uniaxial compliance  $\frac{1}{h_0} \frac{\partial h}{\partial P_{\text{eff}}}$  (Figure 2d) and to express similarly the dependence of  $V_p$  on  $P_{\text{eff}}$  by the coefficient  $\frac{\partial V_p}{\partial P_{\text{eff}}}$  (Figure 2e). As the loading is isotropic, one can assume that  $\frac{\delta V}{V_0} = 3 \frac{\delta h}{h_0}$ , so that the  $P_{\text{eff}}$ -related, “dry” (drained) framework incompressibility  $K_{\text{dry}}$  can be evaluated as

$$-\frac{1}{V_0} \frac{\partial V}{\partial P_{\text{eff}}} = -\frac{3}{h_0} \frac{\partial h}{\partial P_{\text{eff}}}$$

[17] To check the actual reversibility of deformation, the final step of  $P_{\text{eff}}$  applied is also the smallest one (e.g., 1, 2, 3 then 0.5 MPa), and only when the sample expands back for this last step are the two linear coefficients estimated. This procedure is repeated for several values of  $P_c$ , so that several values of the compliance and  $V_p$  sensitivity are derived for varying conditions of  $P_c$  on the same specimen.

### 3.3.3. Plastic Phase

[18] Following the poroelastic response, we increase  $P_{\text{eff}}$  up to values in the range  $1.5 P_{\text{eff}}^{\text{in-situ}} - 2.5 P_{\text{eff}}^{\text{in-situ}}$  during a second phase. This increase results in irreversible compaction, which becomes apparent when releasing  $P_{\text{eff}}$ . For each increment in applied  $P_{\text{eff}}$ , we wait a time sufficient for both deformation and fluid pressure to tend toward asymptotic values. In addition, in each of our samples, for several steps of applied  $P_{\text{eff}}$ , including the largest one, we assess the time necessary for pressure to equilibrate through the sample by applying a differential pressure ( $\sim 1$  MPa) between the sample upper and lower surfaces and letting it decay, similarly to the method for measuring permeability described by *Brace et al.* [1968]. Depending on the sample and on the applied  $P_{\text{eff}}$ , durations required for the pressure difference to decrease down to  $\sim 0.2$ – $0.1$  MPa ranged from a few seconds to  $\sim 2$  h, which led to define the maximum time of our experiments as  $\sim 48$ h.

[19] The amplitude of the irreversible deformation was highly variable and largely depended on the tested material. Irreversible compaction in a sample



such as shown in Figure 2c reached a few percent and was readily apparent in the large change in the slope of the height variations upon application of large  $P_{\text{eff}}$ , which is a traditional way to diagnose the onset of irreversible compaction in consolidation experiments [Casagrande, 1936]. In contrast, the transition between poroelastic and plastic deformation was undecipherable in other samples and final plastic deformation was limited to less than 1%.

[20] There is a choice of variables to express the amount of irreversible deformation (see Table 1). To separate the effects of sample initial resetup in the machine, poroelastic deformation and compaction, the amount of compaction is best estimated within the high-pressure vessel as the normalized reduction in length when  $P_{\text{eff}}$  is increased from  $P_{\text{eff}}^{\text{in-situ}}$  to  $P_{\text{eff}}^{\text{max}}$  (see sample C0001H-5Rvert in section 4.1.3). On the other hand, for some samples, such as shallow ones in Site C0006, a large irreversible deformation started from the smallest application of  $P_{\text{eff}}$ , so that the compaction can be estimated from the normalized length reduction from  $P_{\text{eff}} = 0$  to  $P_{\text{eff}}^{\text{max}}$ , or from the ratio of sample height measured outside of the vessel before and after the experiment.

[21] We does not apply large  $P_{\text{eff}}$  in a single step, but incrementally through successive cycles of increasing amplitude (i.e., up to maximum  $P_{\text{eff}}$ , then back to low  $P_{\text{eff}}$ ; see Figure 2c). This procedure allows us to assess the evolution of the poroelastic coefficients through compaction, by estimating them on the portion of each cycle within the yield surface (in particular in the last step after maximum compaction when  $P_{\text{eff}}$  is released and behavior returns back to the poroelastic field).

### 3.4. Core Material

[22] Core samples from ODP Site 1173 at the Muroto transect (Figure 1) and IODP Sites C0001, C0002, C0006 and C0007 recovered along the Kii transect were available for our experiments (Table 1). The lithology of the samples varies mostly between silts and clays. All of them are constituted principally of clay minerals, with a proportion between 40% and 60%. Due to the proximity of a fossil spreading ridge, temperature gradient is few times larger at Site 1173 than along the Kii transect [Shipboard Scientific Party, 2001].

[23] In spite of these variations, for each site, the samples examined here were collected within homogeneous units (except for the two deepest

samples of C0006 and the deepest one of C0007) to minimize artifacts and allow direct comparison of the test results. We also checked visually the starting material to discard any sample showing macroscopic cracks or other evidence of brittle deformation.

[24] We have tested a total of 31 samples in the isotropic pressure apparatus (Table 1). Most of these specimens were mounted so that properties were measured in a single direction, either “vertical” (longitudinal), i.e., sample long axis is parallel to core axis in ODP/IODP reference frame (C0001, C0002, C0006 and C0007) or “horizontal” (transverse), i.e., sample axis perpendicular to core axis, without further constraint on the direction (Site 1173). For six of them, preparation of two mutually perpendicular cylinders allowed us to estimate the properties in two orthogonal directions (vertical and horizontal). The very low measured anisotropy both in  $V_p$  and poroelastic compliance (see section 4.3) led us to conclude that sample state and properties are relatively independent of the orientation of the samples. As a consequence, all our results are intercomparable and are plotted irrespectively of the measurement direction.

## 4. Results

### 4.1. Mechanical Properties

#### 4.1.1. Correlation of Mechanical State With Other Variables

[25] In Figures 3 and 4 we present poroelastic compliance ( $\frac{1}{h_0} \frac{\partial h}{\partial P_{\text{eff}}}$ ) and plastic deformation ( $h_f/h_0$ ) as a function of porosity (Figures 3a and 4a), in situ effective stress (Figures 3b and 4b) and age (Figures 3c and 4c), for all the tested material, irrespectively of its lithology or site of origin.

##### 4.1.1.1. Poroelastic Moduli

[26] Over the tested samples tested, poroelastic compressibility varies by more than an order of magnitude. Surprisingly, the expected trend of decreasing compressibility with decreasing porosity is weak and seems to vary strongly between the different sites (Figure 3a). Whereas relation between porosity and age is similarly highly scattered (Figure 3c), the compressibility shows a net exponential trend with effective stress (Figure 3b).



**Table 1.** List of Samples From the Nankai Trough Accretionary Complex and Incoming Shikoku Basin Sediments Used in This Study<sup>a</sup>

Sample	Depth (mbsf)	Porosity (%)	P <sub>eff</sub> in Situ (MPa)	T in Situ (°C)	Dir.		Deposition Settings	Lithology	Tectonic Settings	Mineralogy (%)				Uniaxial Compliance		Consolidation			Acoustic Properties	
					h	v				Clay	Qtz	Pl.	Cc.	$\frac{1}{h_0} \frac{\partial h}{\partial P_{eff}}$ (10 <sup>-3</sup> /MPa)	$\frac{h_f}{h_0}$	$\frac{h_{p_{eff}^{max}} - h_{p_{eff}^{in situ}}}{h_0} * 100$	$\frac{h_{p_{eff}^{max}}}{h_0}$	$\frac{\partial V_p}{\partial P_{eff}}$ (km/s/MPa)	V <sub>p</sub> (km/s)	
C0006E-20X	132	48.1	1.1	5.5	X	Tr.	Sandy silt	Front. Thr.	40.9	22.2	21.4	1.2	-7.0	0.911	2.664	0.881	0.070	1.932		
C0006E-25X	180	-	1.6	7.0	X	"	Silty clay	"	26.5	25.9	25.3	1.2	-5.5	0.917	1.926	0.911	0.070	2.099		
C0006E-30X	221	51.5	2.0	8.0	X	"	Silty clay	"	47.4	22.6	21.1	0.5	-5.4	0.892	1.487	0.878		1.972		
C0006E-35X	270	45.0	2.5	9.5	X	"	Silty clay	"	47.9	23.7	20.5	1.7	-6.0	0.923	0.829	0.916	0.035	2.040		
C0006E-42X	343	40.6	3.2	11.5	X	"	Silty claystone	"	43.9	18.0	27.2	1.7	-4.5	0.985	1.505	0.963	0.052	2.058		
C0006E-47X	386	41.0	3.6	12.5	X	"	Silty claystone	"	39.0	21.4	24.7	7.2	-1.2	0.986	0.323	0.983	0.040	2.323		
C0006F-11R	488	45.8	4.6	15.0	X	X	Hemipel.	"	56.4	20.6	15.4	0.7	-1.4	0.997	0.530	0.978	0.023	2.095		
C0006F-19R	563	43.0	5.2	17.0	X	X	"	"	59.7	18.9	10.7	1.5	-3.3	0.998	0.865	0.948	0.035	2.198		
C0001H-1R	232	62.1	1.6	12.0	X	Out. Tr. -W.	Silty clay	Accr. Pr.	50-65	15-25	10-20	0-5	-8.5	0.981	9.150	0.895	0.035	1.733		
C0001H-5R	270	57.5	1.8	14.0	X	X	"	"	50-65	15-25	10-20	0-5	-2.4	0.969	7.739	0.914	0.019	1.767		
C0001H-12R	336	55.3	2.3	17.0	X	"	"	"	50-65	15-25	10-20	0-5	-1.8	0.962	5.504	0.942	0.008	1.815		
C0001H-16R	374	56.1	2.6	18.5	X	"	"	"	50-65	15-25	10-20	0-5	-1.7	0.973	4.008	0.947	0.010	1.912		
C0007C-8X	75	56.0	0.7	5.0	X	Tr.	Silty clay	Front. Thr.	30-55	20-30	20-45	0-5	-12.1	0.921	2.420	0.903	0.034	1.712		
C0007C-10X	90	42.0	0.8	6.0	X	"	Sandy silt	"	30-55	20-30	20-45	0-5	-10.8	0.973	1.820	0.921	0.053	1.812		
C0007D-17R	325	43.0	3.1	16.0	X	"	Silty claystone	"	50-55	22-24	20-25	0-5	-1.2	0.999	0.364	0.977	0.034	1.816		
C0007D-24R	390	50.0	3.7	18.0	X	Hemipel.	Silty claystone	"	60-70	18-22	12-20	0-5	-2.0	1.000	0.806	0.972	0.019	1.956		
C0002B-20R	649	43.0	4.8	25.0		Dis. Bas. Plain	Clayey silt	Fore-arc Bas.	40-55	25-30	20-30	0-5	-1.1	0.996	0.602	0.976	0.034	2.103		
C0002B-44R	875	41.0	6.9	30.0	X	X	Slope apron	"	40-55	15-25	10-30	0-30	-1.4	0.991	0.664	0.972	0.047	2.331		
C0002B-60R	1014	32.0	8.3	34.0		Out. Tr. -W.	Silty clay	Accr. Pr.	45-70	15-30	10-30	0-5	-1.1	0.990	1.429	0.970	0.041	2.626		
1173-28X	254	65.0	1.5	45.0	X	X	Hemipel. (USB)	Silty clay	Oceanward	40-50	30-40	10-20	0-10	-4.5	0.987	4.411	0.947	0.009	1.763	
1173-33X	309	63.0	1.8	55.0	X	X	"	"	40-50	30-40	10-20	0-10	-3.1	0.950	9.078	0.898	0.008	1.744		
1173-38X	350	51.0	2.1	62.0	X	Hemipel. (LSB)	Silty claystone	"	50-60	30-40	0-10	0-5	-4.5	0.967	3.892	0.939	0.027	1.877		
1173-40X	376	50.0	2.3	66.0	X	"	Silty clay	"	50-60	30-40	0-10	0-5	-4.5	0.984	2.538	0.958	0.033	1.897		
1173-44X	408	49.0	2.6	70.0	X	"	Clayey silt	"	50-60	30-40	0-10	0-5	-4.7	0.975	3.209	0.935	0.021	1.906		
1173-49X	455	45.0	3.0	76.0	X	"	Silty claystone	"	50-60	30-40	0-10	0-5	-4.4	0.970	4.669	0.932	0.024	1.985		
1173-51X	479	46.0	3.2	78.0	X	"	"	"	50-60	30-40	0-10	0-5	-3.4	0.958	5.360	0.929	0.022	1.940		
1173-53X	494	42.0	3.3	80.0	X	"	"	"	50-60	30-40	0-10	0-5	-3.8	0.977	2.196	0.952	0.029	2.045		
1173-55X	519	42.0	3.6	83.0	X	"	"	"	50-60	30-40	0-10	0-5	-3.3	0.985	1.637	0.947	0.028	2.049		
1173-59X	550	41.0	3.9	87.0	X	"	"	"	50-60	30-40	0-10	0-5	-2.9	0.988	0.986	0.962	0.027	2.096		
1173-64X	600	38.0	4.4	92.0	X	"	"	"	60-70	20-30	0-10	0-5	-2.2	0.989	0.554	0.963	0.026	2.172		
1173-70X	657	37.0	5.0	98.0	X	X	"	"	40-60	20-30	0-10	var.	-2.9	0.989	1.306	0.959	0.028	2.220		

<sup>a</sup>We estimated porosity  $\phi$  in each of our experimental samples from the combination of our own measurements of loss of weight after drying with shipboard grain density data (moisture and density (MAD) measurements) [Expedition 315 Scientists, 2009a].  $P_{eff}^{in situ}$  is calculated assuming hydrostatic pore pressure. Dir. refers to the direction along which properties were measured, either vertical (v) or horizontal (h). Deposition settings: Hemipel., hemipelagic; Out. Tr. -W., outer trench wedge; Tr., trench; Dis. Bas. Plain, distal basin plain; U(L)SB, Upper (Lower) Shikoku Basin. Tectonic settings: Front. Thr., frontal thrust; Fore-arc Bas., fore-arc basin; Accr. Pr., accretionary prism; Oceanward, seaward of the trench. Consolidation, i.e., height variations associated to the application of a large  $P_{eff}$  (of the order of 1.5 to 2.5  $P_{eff}^{in situ}$  depending on the site considered) is indicated by several indexes:  $\frac{h_f}{h_0}$  is the ratio of sample heights measured out of the pressure vessel before and after the whole experiment,  $\frac{h_{p_{eff}^{max}} - h_{p_{eff}^{in situ}}}{h_0} * 100$  is the normalized height reduction measured within the chamber between  $P_{eff}^{in situ}$  and  $P_{eff}^{max}$ , and  $\frac{h_{p_{eff}^{max}}}{h_0}$  is the ratio of height for  $P_{eff}^{max}$  (measured in the chamber) over initial height (measured outside).

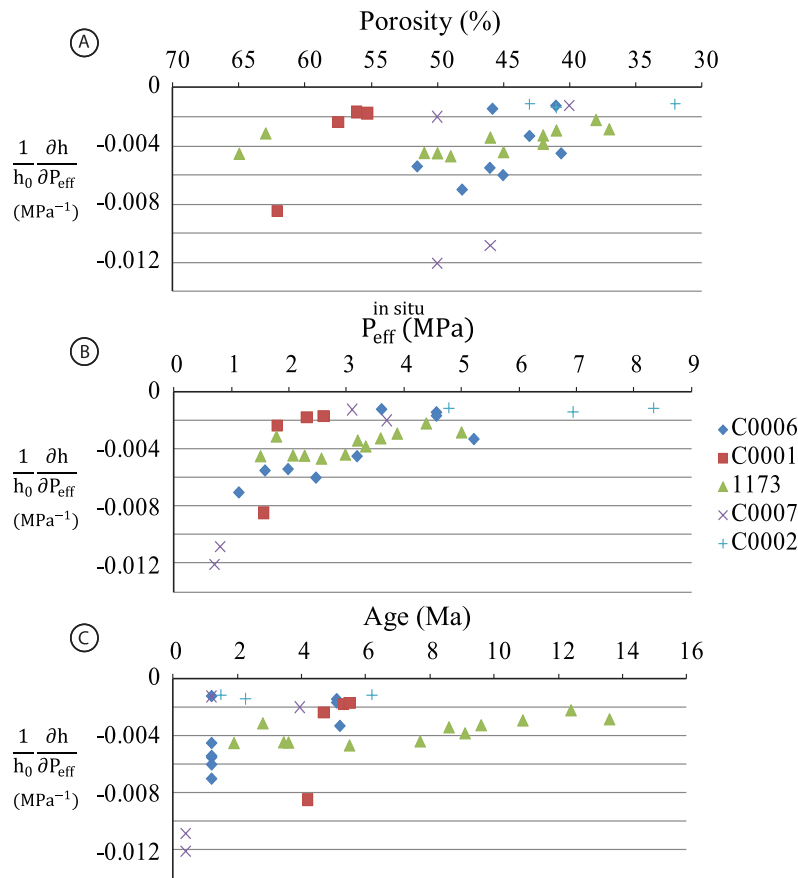


**Figure 3.** Poroelastic uniaxial compliance  $\frac{1}{h_0} \frac{\partial h}{\partial P_{\text{eff}}}$  determined in the different Sites C0001, C0002, C0006, and C0007 of IODP Legs 315 and 316 and Site 1173 of ODP Leg 190, as a function of (a) porosity, (b) in situ  $P_{\text{eff}}$  calculated assuming hydrostatic pore pressure, and (c) age.

#### 4.1.1.2. Irreversible Deformation

[27] The extent of irreversible compaction (estimated from the ratio of sample height measured outside of the vessel before and after the experiment) in response to a load increase over in situ conditions, i.e., to the application of  $P_{\text{eff}}$  in the range 1.5~2.5  $P_{\text{eff}}^{\text{in-situ}}$ , shows large differences within the tested samples. We observe a wide range of sediment response from virtually no compaction to irreversible shortening larger than 10% (Figure 4). The resistance to compaction is better correlated with  $P_{\text{eff}}^{\text{in-situ}}$  (Figure 4b) than with either age (moderately good agreement, see Figure 4c) or porosity (poor correlation; see Figure 4a), suggesting that the sample plastic behavior and yield strength is closely tied to in situ stress conditions.

#### 4.1.2. Site-by-Site Depth Evolution of the Material Mechanical State

[28] The general strengthening with depth can be further analyzed site by site, i.e., for lithologically

homogeneous sediments (Figure 5). Such strengthening is reflected both in a decrease in poroelastic compliance and in a decrease in irreversible deformation (normalized reduction in length from  $P_{\text{eff}}^{\text{in-situ}}$  to  $P_{\text{eff}}^{\text{max}}$  for Site 1173 and from  $P_{\text{eff}} = 0$  to  $P_{\text{eff}}^{\text{max}}$  for Site C0006, see section 3.3.3), which are restricted to a rather narrow depth interval, whose precise position varies between sites. For Site C0006 (as well as C0007, see Figures 3 and 4), located at the toe of the prism, the threshold overburden stress causing the change in strengthening occurs between 2.5 and 3 MPa, while at the Shikoku Basin Site 1173, it appears to kick in at ~4 MPa (see Figure 4b).

#### 4.1.3. Consolidation Behavior

[29] The consolidation curves of samples C0001H-5H, C0007C-8X and C0007D-17R (Figure 6) are representative of all the samples we tested. The mechanical response to the experimental consoli-

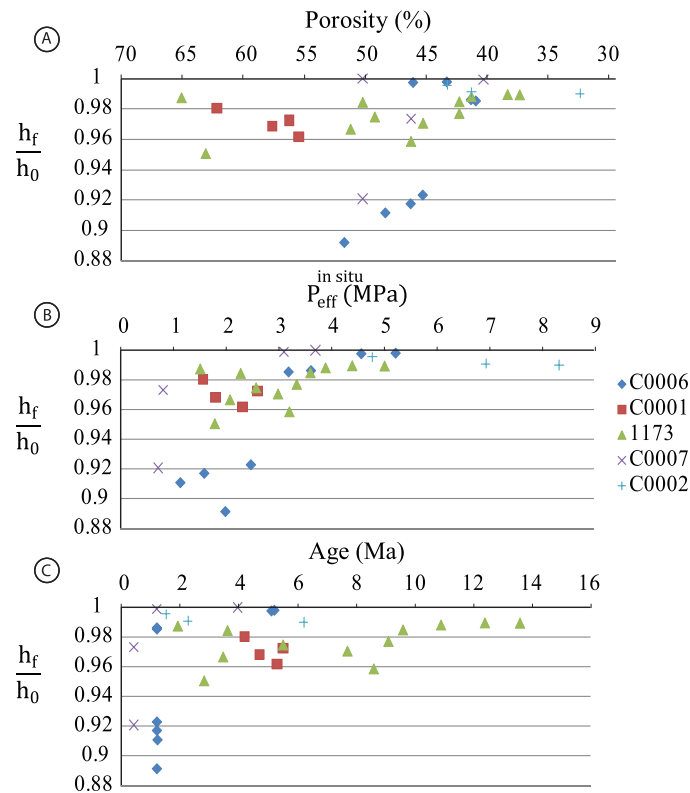


**Figure 4.** Irreversible shrinkage, measured as the final height  $h_f$  normalized by the initial one  $h_0$  (both measured out of the pressure vessel) after a test where  $P_{eff}$  was applied up to values between  $1.5 P_{eff}^{in-situ}$  and  $2.5 P_{eff}^{in-situ}$  in the different Sites C0001, C0002, C0006, and C0007 of IODP Legs 315 and 316 and Site 1173 of ODP Leg 190, as a function of (a) porosity, (b) in situ  $P_{eff}$  calculated assuming hydrostatic pore pressure, and (c) age.

dation can be schematically divided into two end-members: while shallow samples (C0001H-5H, C0007C-8X) were affected by a large irreversible deformation, deep samples (C0007D-17R) were hardly deformed (Figure 6). In addition, within shallow deformable samples, we observed two contrasted kinds of behavior: sample C0001H-5H was affected by irreversible compaction only when  $P_{eff}$  exceeded a threshold of the order of  $P_{eff}^{in-situ}$ . In contrast, sample C0007C-8X showed the most intense shrinkage upon the application of the initial step of  $P_{eff}$ , i.e., for  $P_{eff}$  much lower than in situ value.

#### 4.2. $V_p$ Controlling Factors

[30] In addition to the direct mechanical response, we also assessed  $P$  wave velocity evolution as a function of increasing effective (Figure 7) and confining (Figure 8) stresses. Although  $P$  wave arrival time was undecipherable without applying  $P_{eff}$  and  $P_c$ , for values as low as a few hundred kPa,

the signal was sufficiently strong to estimate  $V_p$  and its dependence on  $P_{eff}$  and  $P_c$ .

##### 4.2.1. $P_{eff}$ Dependence

[31] During poroelastic (reversible) deformation and fluid expulsion (see above and Figure 2), an increase in  $P_{eff}$  results in stiffening of the structure expressed by an increase in compressional wave velocity (Figure 7a), which is close to linear in the range 0.5–3 MPa for deep samples (ca. > 300 mbsf) and 0.5– $P_{eff}^{in-situ}$  for shallow samples (<300 mbsf), similarly to poroelastic moduli. This linear approximation breaks down at large  $P_{eff}$  (~10 MPa), where  $V_p$  tends asymptotically toward a constant value, as well as at very low  $P_{eff}$  (<0.5 MPa), where  $V_p$  variations with  $P_{eff}$ , hence the coefficient  $\frac{\partial V_p}{\partial P_{eff}}$ , get larger.

[32] Values of  $\frac{\partial V_p}{\partial P_{eff}}$  compiled over the drill sites studied are preferentially concentrated in the range 0.02~0.04 km/s/MPa (Figure 7b). In contrast to poroelastic moduli,  $\frac{\partial V_p}{\partial P_{eff}}$  does not seem to be correlated with depth in the samples analyzed.

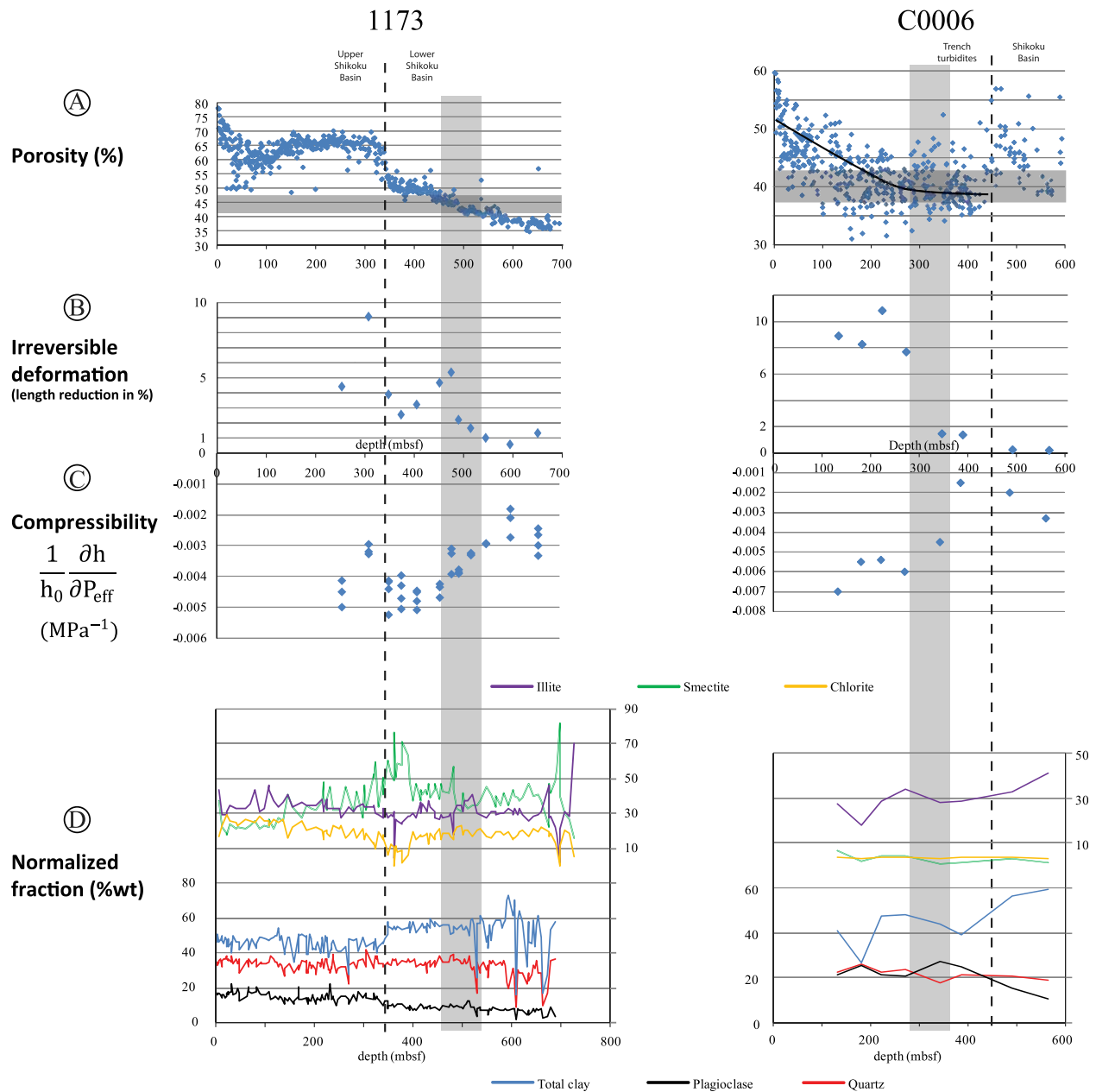


**Figure 5.** Variations with depth in physical properties and composition for Sites 1173 (ODP Leg 190) and C0006 (IODP Leg 316): (a) porosity, (b) plastic shrinkage after application of  $P_{eff}$  in the range  $1.5 P_{eff}^{in-situ} - 2.5 P_{eff}^{in-situ}$ , (c) poroelastic coefficient, and (d) composition determined by XRD. In both sites there is a rapid strengthening around some depth interval (vertical gray band), evidenced by a decrease in poroelastic compliance and plastic deformation. These variations in mechanical strength, not correlated with any sharp change in composition, are rather the result of the combined action of cementation/decrease of the porosity down to some “critical” value corresponding to compact state. (Note for XRD data: (Site 1173) the proportions of the clay minerals are determined only for the particles with a size < 2 microns and are normalized with respect to total clay [Shipboard Scientific Party, 2001; Steurer and Underwood, 2005]. Site C0006: the clay mineral proportions are normalized with respect to the bulk composition. The “smectite” content is in fact smectite + montmorillonite content.)

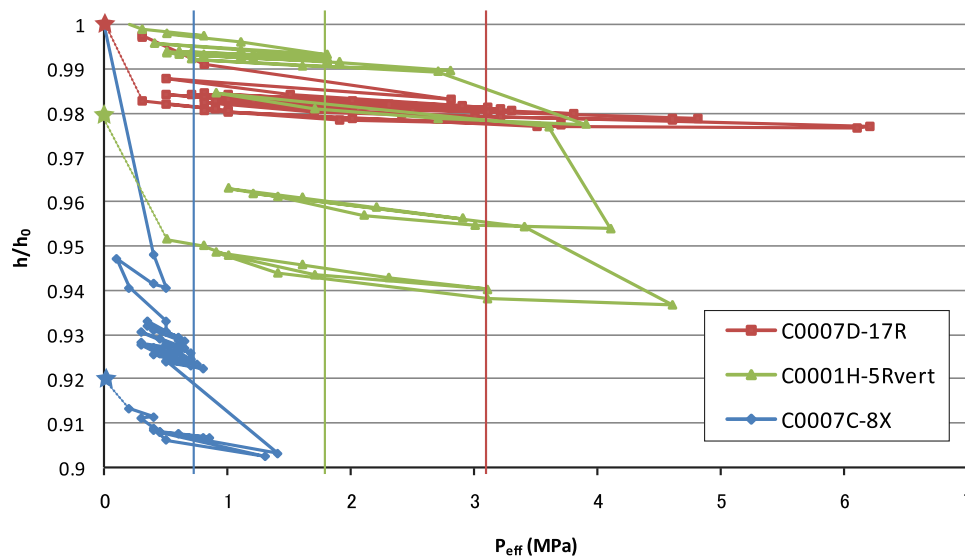


**Figure 6.** Typical patterns of mechanical response to an applied effective pressure larger than  $P_{\text{eff}}^{\text{in-situ}}$ . C0001H-5Rvert (green) and C0007C-8X (blue) are affected by a significant amount of irreversible shrinkage, which is virtually absent during C0007D-17R (red) deformation. Such plastic deformation is nevertheless very different between samples C0001H-5Rvert and C0007C-8X; in C0007C-8X, most of irreversible deformation occurs upon the first steps of  $P_{\text{eff}}$  application, even for values lower than  $P_{\text{eff}}^{\text{in-situ}}$  (vertical bars). In contrast, in sample C0001H-5Rvert, the response to deformation remains mostly poroelastic until  $P_{\text{eff}}$  reaches values close to  $P_{\text{eff}}^{\text{in-situ}}$ , from where irreversible compaction starts. Stars correspond to final normalized height measured out of the pressure vessel while all other points are measured within the vessel. Note the large variations between the three samples in the elastic rebound, i.e., the change in height (hence porosity) in the last phase of each experiment upon release of the pressures from in situ conditions.

#### 4.2.2. $P_c$ Dependence

[33] By interpolating  $V_p$  to a constant  $P_{\text{eff}}$  (arbitrarily chosen to be 3 MPa) for various  $P_c$  in the domain of poroelastic deformation, we assessed the possible effect of confining pressure on  $V_p$  (Figure 8). The quality of the obtained trend varies between samples, but the slope  $\frac{\partial V_p}{\partial P_c}$  is in the range  $1.2\text{--}1.8 \cdot 10^{-3}$  km/s/MPa, yielding a correction to be applied to onboard measurements to restore them to in situ  $P_c$ . For samples from the vicinity of the trench such as Site 1173, where almost 5 km of water lie above seafloor, this correction is of the order of 0.1 km/s, i.e., nonnegligible.

#### 4.3. Anisotropy of Acoustic and Mechanical Properties

[34] Both uniaxial compliance and  $V_p$  (determined for in situ conditions) show very similar values in the two perpendicular directions for most of the samples (Figures 9a and 9c). When a difference between the pair of experiments is observed, it does not show any systematic pattern. Although the small number of samples tested prevents us from drawing conclusions on a site-by-site basis, our

data attest to the very limited anisotropy of the material recovered a few hundred meters below the seafloor regardless of its position in the margin.

## 5. Discussion

### 5.1. Core/Log/Seismic Integration

#### 5.1.1. Correction Factors to In Situ Conditions

[35] As the majority of  $V_p$  measurements on core samples are performed in the laboratory, corrections to restore  $V_p$  to in situ conditions are necessary. On the basis of submersible-assisted measurements of  $V_p$ , *Hamilton et al.* [1970] and *Hamilton* [1971a] derived for subseafloor sediments correction factors for salinity, temperature and confining pressure. In addition, for deeper sediments, effective pressure is an additional variable likely to play a role on  $V_p$ , involving another correction factor [e.g., *Hoffman and Tobin*, 2004]. Our experiments for various conditions of  $P_p$  and  $P_c$  provide the opportunity to assess the correction factors to be applied to sediments down to  $\sim 1000$  mbsf.

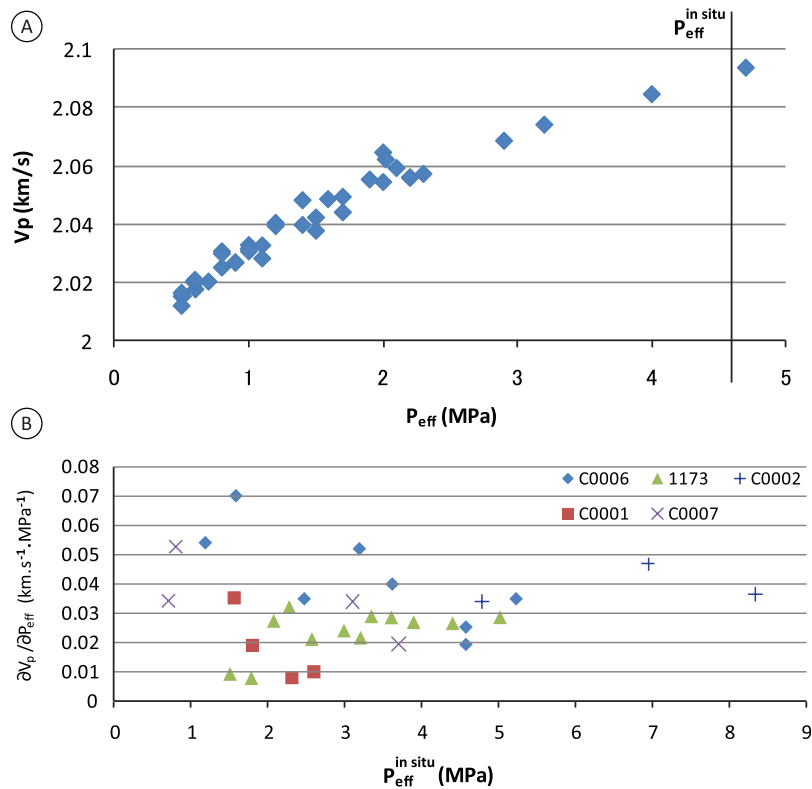


**Figure 7.** (a) Linear dependence of  $V_p$  on effective pressure during poroelastic (reversible) deformation of sample C0006F-11R. (b) Compilation of  $\frac{\partial V_p}{\partial P_{eff}}$  over several sites (abscissa  $P_{eff}^{in-situ}$  estimated for hydrostatic pore pressure).

### 5.1.1.1. $P_c/P_p$ Dependence

[36] The simplest poroelastic model of our samples consists of an incompressible, fluid-saturated solid skeleton whose geometry is the sole function of  $P_{eff}$ . In such a framework, the porosity is inde-

pendent of  $P_c$  for a given  $P_{eff}$ , which is in agreement with our measurements of sample height for various  $P_c$ . Regardless of porosity variations, an increment of  $P_c$  results in an increase in fluid pressure at a given  $P_{eff}$ ; since the sample is incompressible, this leads to an increase in  $V_p$ . The

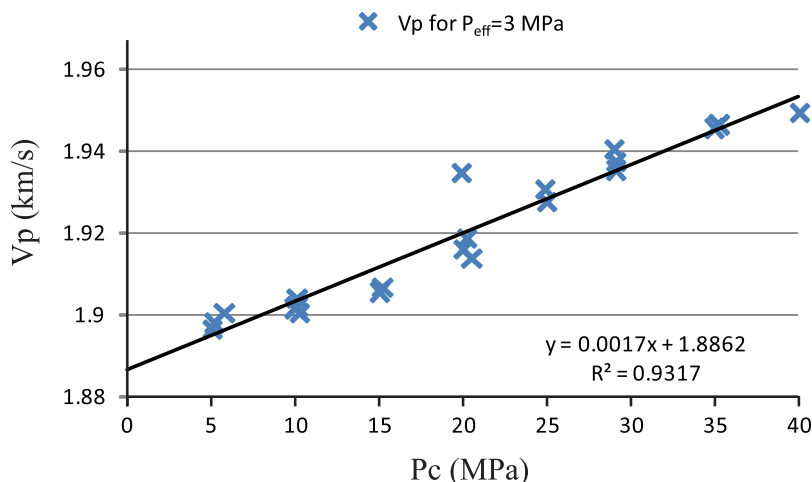


**Figure 8.**  $V_p$  dependence on  $P_c$  in core sample C0001H-16R. For each step of  $P_c$  (i.e., each elementary step of phase 1, where deformation is reversible),  $V_p$  was estimated for a given  $P_{eff}$  (arbitrarily chosen to be equal to 3 MPa), using the regression law described in Figure 2e.

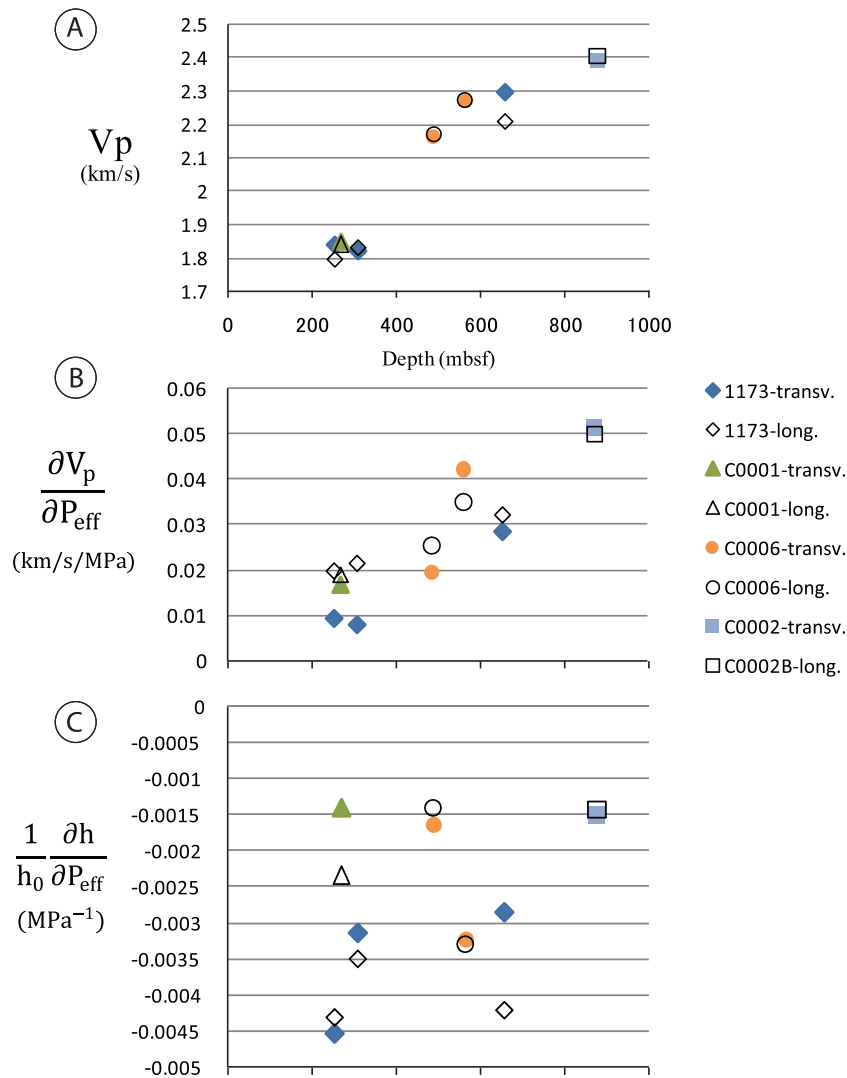


**Figure 9.** Anisotropy of (a, b) acoustic and (c) mechanical properties. For each core sample, two cylindrical pieces were prepared, with the axis of the cylinder (hence the direction of measurement) orientated either parallel to core axis (longitudinal samples/properties) or perpendicular to it (transverse samples/properties). Samples with horizontal axis were not orientated in the geographical system.

magnitude of such an increase depends on the saturated (“undrained”) moduli  $K_{sat}$  and  $\mu_{sat}$  [Mavko *et al.*, 2009], which can in turn, using Gassmann’s [1951] substitution equations, be expressed in terms of dry (“drained”) framework incompressibility  $K_{dry}$  and shear modulus  $\mu_{dry}$  and fluid incompressibility  $K_f$ . Saturated shear modulus is simply

$$\mu_{sat} = \mu_{dry}$$

For near-incompressible solid grains, i.e., with incompressibility much larger than framework incompressibility (assumption justified by the

values measured in our samples, see section 5.2.2), incompressibility  $K_{sat}$  can be approximated by

$$K_{sat} = K_{dry} + \frac{K_f}{\phi},$$

with  $\phi$  the porosity.

[37] Such saturated poroelastic moduli combine to give the velocity as

$$V_p = \sqrt{\frac{K_{sat} + 4/3\mu_{sat}}{\rho}}$$



The effect of an increment in fluid pressure  $P_p$  on  $V_p$  operates through an increase in both  $K_f$  and fluid density  $\rho_f$ , yielding

$$\begin{aligned}\frac{\partial V_p}{\partial P_p} &= \frac{\partial}{\partial P_p} \sqrt{\frac{K_{\text{sat}} + 4/3\mu_{\text{sat}}}{\rho}} = \frac{\partial}{\partial P_p} \sqrt{\frac{K_{\text{sat}} + 4/3\mu_{\text{sat}}}{\rho_s(1-\phi) + \rho_f\phi}} \\ &= -\frac{V_p\phi}{2\rho} \frac{\partial \rho_f}{\partial P_p} + \frac{1}{2\phi\rho V_p} \frac{\partial K_f}{\partial P_p} \\ &= -\frac{V_p\phi}{2\rho} \frac{\rho_f}{K_f} + \frac{1}{2\phi\rho V_p} \frac{\partial K_f}{\partial P_p}.\end{aligned}$$

Taking average values of  $V_p = 1.9$  km/s,  $\phi = 0.5$ ,  $\rho = 1850$  kg/m<sup>3</sup>,  $K_f(\text{atm pressure}) = 2.34$  GPa and  $K_f(100\text{MPa}) = 2.98$  GPa [Knauss, 2005] we obtain

$$\frac{\partial V_p}{\partial P_p} = 1.7 \cdot 10^{-3} \text{ km/s/MPa}$$

[38] These values are very similar to the experimental findings (Figure 8), which confirms that our  $P_c$  dependence of  $V_p$  actually reflects the effect of variations in pore fluid pressure on velocity. For practical purpose, as the actual in situ fluid pressure is not known, in samples such as ours where the effective pressure is limited to low values, one can use, instead of the fluid pressure, the confining pressure  $P_c$  to derive the correction, which is not negligible for the deep-sea rocks considered here.

### 5.1.1.2. Temperature Dependence

[39] Temperature variations between laboratory (23°C) and in situ conditions induce variations in density and elastic moduli, hence a correction on velocity is a priori necessary. We do not have experimental data as regards the effect of temperature, but we can apply the simple model developed above, yielding, for the temperature dependence,

$$\frac{\partial V_p}{\partial T} = -\frac{V_p\phi}{2\rho} \frac{\partial \rho_f}{\partial T} + \frac{1}{2\phi\rho V_p} \frac{\partial K_f}{\partial T},$$

with  $\frac{\partial K_f}{\partial T} \approx 10$  MPa/°C [Knauss, 2005] and  $\frac{\partial \rho_f}{\partial T} \approx 0.17$  kg/°C [Fofonoff, 1985]. Taking again as average values  $V_p = 1.9$  km/s,  $\phi = 0.5$  and  $\rho = 1850$  kg/m<sup>3</sup> yields a correction for the temperature of  $\frac{\partial V_p}{\partial T} \approx 0.00318$  km/s/°C. For example, for sub-seafloor sediments ( $\Delta T = 1.5 - 23 = -21.5$ °C), the temperature correction is  $-0.068$  km/s, really close to the correction given by Hamilton [1971a] of  $-0.074$  km/s, which was derived for ocean water.

For each of our sample, we estimated the temperature correction using their respective  $V_p$ ,  $\phi$  and  $\rho$ , which we determined in the laboratory, as well as their in situ temperature (values in Table 1, estimated from the gradients given by *Shipboard Scientific Party* [2001], *Expedition 315 Scientists* [2009b, 2009c], and *Expedition 316 Scientists* [2009a, 2009b]).

### 5.1.1.3. $P_{\text{eff}}$ Dependence

[40] We derived experimentally in the range 0.5–3 MPa a linear coefficient  $\frac{\partial V_p}{\partial P_{\text{eff}}}$  to account for the variations in  $V_p$  with effective pressure. To restore atmospheric pressure  $V_p$  to  $P_{\text{eff}}^{\text{in-situ}}$ , the sole correction  $\frac{\partial V_p}{\partial P_{\text{eff}}} \times P_{\text{eff}}^{\text{in-situ}}$  is insufficient, as  $V_p$  decrease for low  $P_{\text{eff}}$  are larger than predicted by the linear correction [e.g., Tobin and Moore, 1994]. For the sake of simplicity, we defined the additional correction as a constant  $\Delta V_p$ :

$$V_p^{\text{in-situ}} = V_p^{\text{in-air}} + \frac{\partial V_p}{\partial P_{\text{eff}}} P_{\text{eff}}^{\text{in-situ}} + \Delta V_p,$$

which we roughly estimated in our samples. Similarly to  $\frac{\partial V_p}{\partial P_{\text{eff}}}$  (Figure 7), values of the constant correction  $\Delta V_p$  are quite variable between samples. Nevertheless, if we try to establish general corrections for effective pressure, we can define two distinct categories of samples. “Cemented” samples (see below section 5.2.3) have very low  $\frac{\partial V_p}{\partial P_{\text{eff}}}$  ( $\approx 0.01$  km/s/MPa) and  $\Delta V_p$  ( $\approx 0$ –0.05 km/s). “Uncemented” samples have larger  $\frac{\partial V_p}{\partial P_{\text{eff}}}$  (0.02–0.05 km/s/MPa) and  $\Delta V_p$  ( $\approx 0.05$ –0.1 km/s). These values have to be considered with caution, as they are unlikely to be relevant to a large range of lithologies and settings (e.g., the larger correction in carbonate-rich sediments by *Urmos and Wilkens* [1993]). It is nevertheless certain that the correction to be applied cannot be constant and has to depend on effective pressure.

### 5.1.1.4. Validity of Our Experimental Measurements

[41] The corrections determined above enable us to check whether our experimental  $V_p$  match shipboard core velocities (measured at atmospheric pressure and ambient temperature). For this purpose, we must for each of our sample (1) extrapolate our experimental  $V_p$  down to  $P_{\text{eff}} = 0$  and (2) apply a correction to reduce  $P_p$  down to zero. Among the various holes studied, Site 1173 is the one where the most numerous atmospheric pressure core  $V_p$  data are available. Our experimental velocities, restored to atmospheric pressure condi-

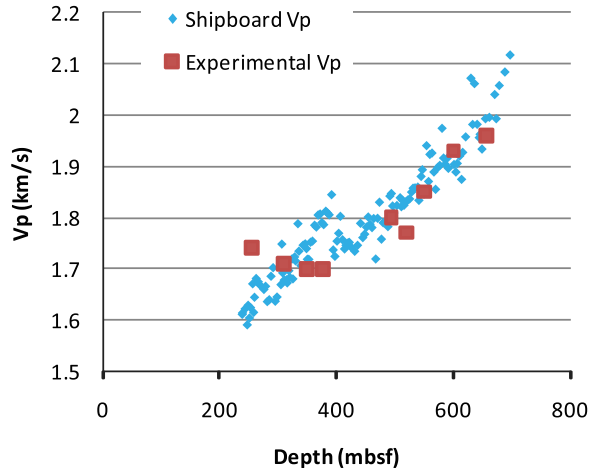


**Figure 10.** Comparison of compressional velocities  $V_p$  either (1) measured onboard on core samples (diamonds), i.e., for  $P_c = 0$  and  $P_{eff} = 0$ , or (2) estimated in our experiments (squares) as the limit for  $P_{eff} = 0$  and corrected to  $P_c = 0$  (see text for description). Measurements from both data sets were performed at ambient temperature ( $\sim 20^\circ\text{C}$ – $25^\circ\text{C}$ ).

tions, are in close agreement with  $V_p$  determined at atmospheric pressure (Figure 10), attesting to the validity of our measurements and of the corrections we derived from them. This further shows that the difference in pulse frequency (500kHz for shipboard core velocity [Blum, 1997], 3MHz for our device) does not induce significant velocity dispersion, even if the frequency we used is slightly over 1MHz, the limit usually considered for neglecting velocity dispersion [Kibblewhite, 1989].

#### 5.1.1.5. Matching Laboratory With In Situ $V_p$

[42] The restoration of compressional wave velocities measured in the laboratory to in situ conditions requires the addition of corrections for temperature, fluid ( $\approx$  confining) and effective pressures defined above:

$$V_p^{in-situ} \approx V_p^{in-air} + \frac{\partial V_p}{\partial T} \Delta T + \frac{\partial V_p}{\partial P_p} P_p + \frac{\partial V_p}{\partial P_{eff}} P_{eff}^{in-situ} + \Delta V_p.$$

As noted by Hamilton [1971a], for  $P_c$  of the order of 50 MPa, the corrections for temperature and pore fluid pressure, of opposite sign and of similar amplitude, cancel out, so that they can be neglected. For settings with much shallower ocean, e.g., forearc basin sediments, this is not the case and the corrections must be carefully assessed.

#### 5.1.2. Comparison of Laboratory-Derived Data With Logging/Seismic Data

[43] Concomitant core sampling and logging while drilling provide an excellent basis to determine (2)  $V_p$  for in situ conditions using logging tools and (2)  $V_p$  at atmospheric pressure (i.e., null effective pressure) directly on core samples in the same lithology. From the average mismatch between core and logging  $V_p$  (based on the comparison of onboard  $P$  wave velocities on discrete samples with wireline DSI data in the borehole), Hoffman and Tobin [2004] derived an average correction to be applied to restore core velocities to in situ conditions. This correction relies on the assumption that logging and discrete core  $V_p$ , although determined at different frequencies and over different representative volumes, are the same. The problem can be considered the other way round and one can check whether in situ  $V_p$  determined by distinct methods (core/logging/check shots/seismic) coincide or not.

[44] The lack of knowledge of  $P_{eff}^{in-situ}$  severely hampers a precise estimate of in situ  $V_p$  for core samples; a priori, only a range of values, bounded by the two end-member cases (hydrostatic or lithostatic  $P_{eff}$ ), can be assessed (Figure 11). Nevertheless, indirect arguments as well as direct measurements (see section 3.3) support the idea that the actual effective pressure is close to hydrostatic pressure.

[45] Our laboratory-determined data (corrected for the temperature difference) are in average higher than other kinds of velocities, with a difference in the range 0.05–0.3 km/s for hydrostatic pore fluid conditions (Figure 11). We have no definite explanation for the systematic discrepancy between core and logging velocities. As logging  $V_p$  relies on waves with a much larger wavelength than laboratory measurement, one possible cause to this discrepancy is velocity dispersion, although there is no consensus on both its amplitude and underlying microscopic processes [Best et al., 2001; Gorgas et al., 2002; Hamilton, 1971b; Kibblewhite, 1989; Robb et al., 2007]. One can note that our measurements are in agreement with shipboard velocities (Figure 10), so that dispersion, with respect to logging  $V_p$ , should also affect shipboard core  $V_p$ . A second factor can contribute to lower logging velocities with respect to core velocities; the larger the wavelength, the larger the size of the representative elementary volume, hence the larger the range of size of the defects (faults, zones of weak material) potentially lowering the velocities. This can explain why measurements on

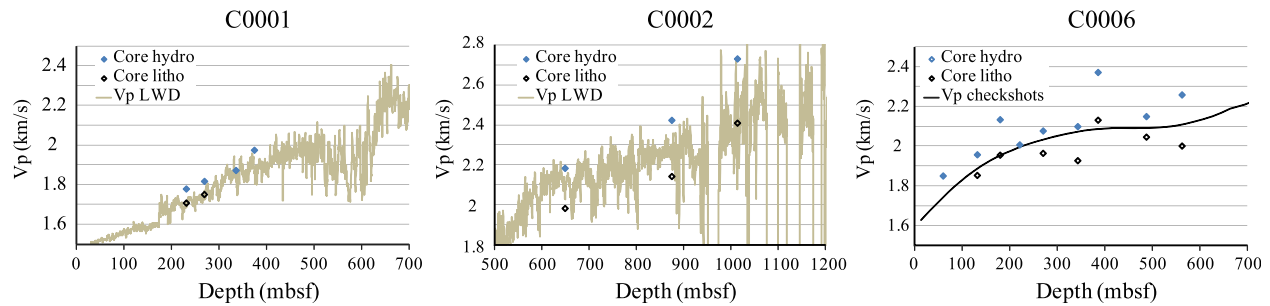


**Figure 11.** Comparison of  $V_p$  experimentally determined on core sample with logging data acquired during drilling: (left) Site C0001, (middle) Site C0002, and (right) Site C0006. Experimental  $V_p$  were assessed for in situ conditions of temperature and pressure, i.e.,  $P_c$  equal to the overlying sedimentary load,  $P_p$  equal either to hydrostatic (direct measurement), or lithostatic (extrapolation using experimental regression coefficients) conditions. Logging data correspond to logging while drilling (Sites C0001 and C0002) or check shot (Site C0006) [Expedition 314 Scientists, 2009].

cm-scale “strong” samples yields higher velocities than logging measurements that necessarily incorporate faults and weak zones. In this respect, velocity data derived from check shots from the surface (Site C0006), where the seismic source and the receiver are distant by a thousands of meters, are likely to be more affected than logging data acquired with the LWD SonicVisionTool (Sites C0001 and C0002), where source and receiver are  $\sim 3$  m apart [Expedition 314 Scientists, 2009].

### 5.1.3. $V_p$ Versus Porosity Relationship

[46] In order to compare core and logging/check shot  $V_p$  over the different sites, we determined  $V_p$  versus porosity curves for all data sets *for* in situ conditions (see Appendix A for a description of the data used). As a result (Figure 12), for  $\phi$  in the range  $\sim 0.3$ – $0.6$ ,  $V_p$  versus porosity points from cores of all sites cluster along a single trend. This shows that velocities, for high-porosity material, do not depend at first order on composition/clay fraction, as was already noted by *Erickson and Jarrard* [1998].

[47] Most of the logging data plot along the same trend, but for C0002 and C0004 (unit IV) where velocities are higher and C0001 (unit I) where they are lower. The interpretation of these discrepancies between core and logging data is quite complicated, as they combine potential errors on both velocity and porosity data. Plots of our rebound-corrected sample porosity with resistivity-derived porosity shows significant differences (Appendix A), that may account for most of the discrepancy between logging and core data in Figure 12.

[48] Our experimentally derived  $V_p$  versus porosity relationship is close to *Erickson and Jarrard's*

[1998] “high-consolidation” curve, but departs significantly from their “normal consolidation” curve as well as from *Hoffman and Tobin's* [2004] relationship. One possible reason is that the correction ( $+0.043 \pm 0.029$  km/s) applied by *Hoffman and Tobin* [2004] to restore atmospheric pressure data to in situ conditions is smaller than the correction we derived above to account for the increase in pore fluid and effective pressure. As  $V_p$  versus porosity curves are often used to estimate properties at depths larger than drilling depth range, for example pore pressure [e.g., *Tobin and Saffer*, 2009], the choice of the curve has potentially significant consequence: a shift in  $V_p$  versus porosity relationship by  $+0.1$  km/s results in decrease in estimated pore pressure by  $\sim 0.6$  MPa (see Appendix B), which is nonnegligible for the relatively shallow rocks ( $<1000$  mbsf) considered here.

## 5.2. Sensitivity of $V_p$ to Material Physical Changes

### 5.2.1. Variations in $V_p$ During Consolidation

#### 5.2.1.1. $V_p$ Versus $\phi$ Evolution During Experimental Consolidation

[49] Following earlier workers' analysis [*Karig*, 1996; *Karig and Ask*, 2003], some insights on the consolidation state of Nankai sediments can be gained from the comparison of the characteristics of in situ and experimental compaction. For the sake of simplicity, we consider only small variations around which porosity evolution can be approximated by a linear relationship as

$$C = \frac{\partial \phi}{\partial P_{\text{eff}}}$$

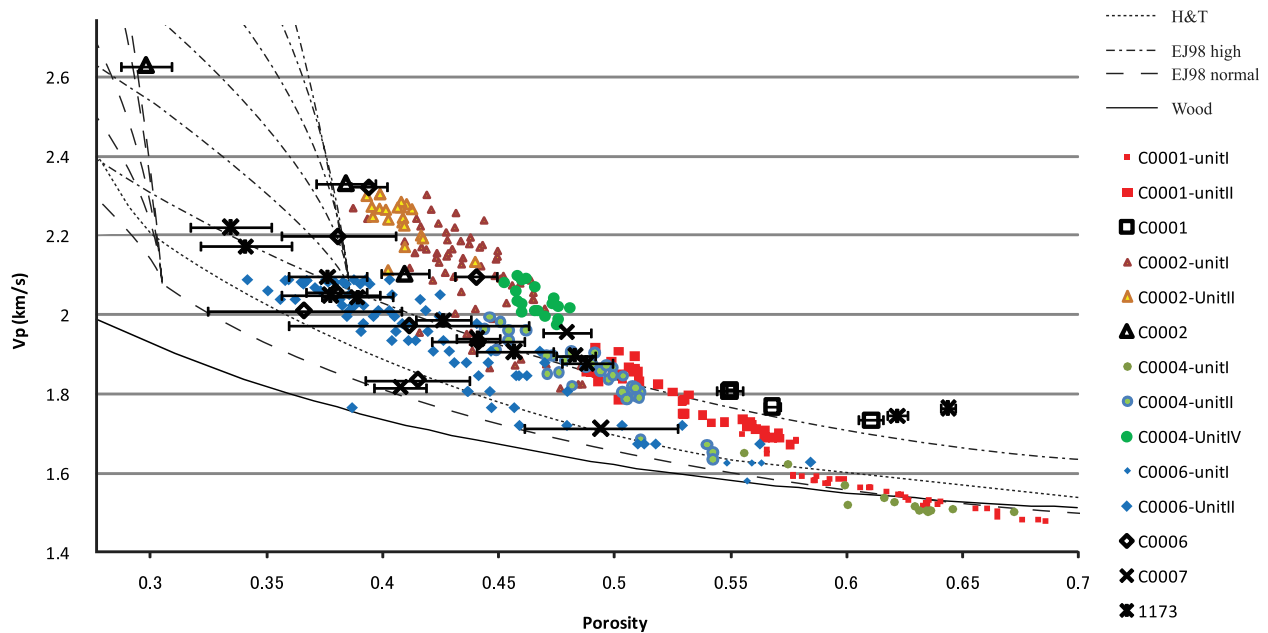


**Figure 12.**  $V_p$  as a function of porosity. Color symbols pair resistivity-derived porosity with LWD  $V_p$  for Sites C0001, C0002, C0004, and with check shot  $V_p$  for C0006 (see *Expedition 314 Scientists* [2009] for method description). Hollow symbols pair laboratory-measured  $V_p$  for  $P_c$  equal to the overlying sedimentary load,  $P_p$  equal to hydrostatic conditions and ambient  $T$  with porosity of our experimental material estimated by combining our own measurements of water loss upon drying with onboard data of solid grain density and adding a correction for rebound (see Appendix A). H&T, *Hoffman and Tobin's* [2004] empirical law; EJ98 high (normal), *Erickson and Jarrard's* [1998] empirical law for high (normal) sediment consolidation; Wood, *Wood's* [1941] suspension model calculated for incompressible solid grains and water rigidity at  $P = 50$  MPa and  $T = 1.5^\circ\text{C}$ .

[50] As detailed in section 3.2, we did not precisely estimate porosity variations and can only infer them from height variations. Taking the isotropic assumption ( $\frac{\Delta V}{V} / \frac{\Delta h}{h} = 3$ ) as a maximum estimate, we estimated the porosity variations in sample C0006E-30X (~220 mbsf) along the experimental consolidation curve. As a result of the application of an increasingly large  $P_{\text{eff}}$ , irreversible shrinkage occurred, with porosity variations  $\Delta\phi = 2\%$  for a variation of  $P_{\text{eff}}$  of 1 MPa, which can be roughly converted into  $\Delta\phi = 2\%/100$  m (Figure 13a). A similar relationship  $\frac{\Delta\phi}{\Delta P_{\text{eff}}}$ , or  $\frac{\Delta\phi}{\Delta z}$  can be deduced from in situ variations of porosity. In situ compaction curve at Site C0006 calculated on core samples (porosity from moisture and density (MAD)) [*Expedition 316 Scientists*, 2009a] in the depth range 50–250 mbsf yielded a porosity decrease of the order of  $\Delta\phi = 4\%/100$  m. The factor two of difference between experimental and in situ compaction trends suggests that, in addition to instantaneous compaction, a significant proportion of in situ porosity decrease results from time-dependent processes and that the short durations of experimental consolidation did not allow such processes to be active. Although *Saffer* [2003] obtained for Nankai samples consolidation trends

similar for experimental and in situ conditions, one may note, however, that this is not commonly the case, because in many consolidation experiments, coefficients  $\frac{\Delta\phi}{\Delta P_{\text{eff}}}$  are an order of magnitude lower than for in situ consolidation curves [*Karig and Ask*, 2003].

[51] In parallel to the porosity decrease, we observed, associated with the irreversible deformation undergone by this particular sample, an increase in velocity, which can be estimated as  $\Delta V_p \approx 6.10^{-2}$  km/s for  $\Delta P_{\text{eff}} = 1$  MPa (Figure 13b). Combining porosity and velocity variations trends yields the experimental  $V_p$  versus  $\phi$  relation as

$$\frac{\Delta V_p}{\Delta\phi} = 3 \cdot 10^{-2} \text{ km/s/\%}.$$

[52] This trend, calculated on a single sample experimentally consolidated, is relatively similar to our “in situ”  $V_p$  versus  $\phi$  relationship in Figure 13, which is derived by estimating in situ  $V_p$  and porosity in many samples from various depths. This good agreement between experimental and in situ compaction trends shows that the increase in  $V_p$  with depth is mostly the result of mechanical

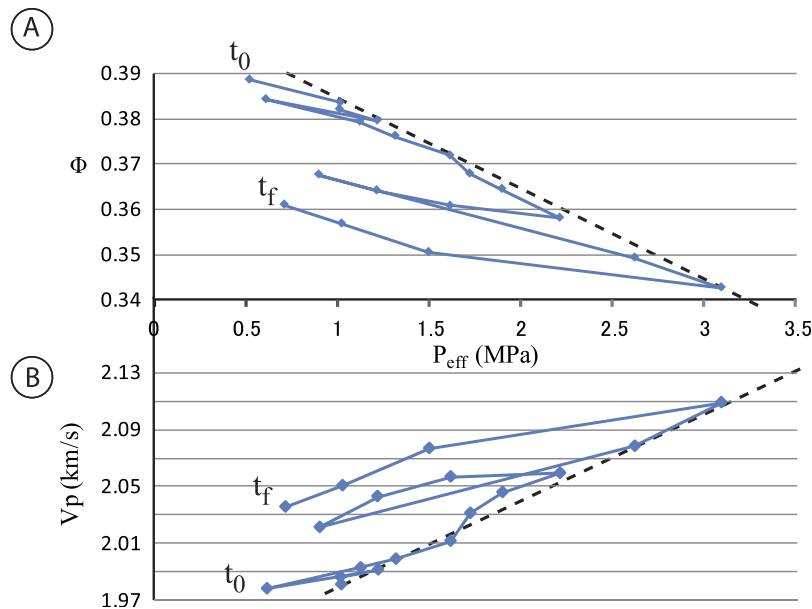


**Figure 13.** (a) Determination of experimental compaction curves  $\phi = \text{func}(P_{\text{eff}})$  for sample C0006E-30X (~220 mbsf). The porosity variations are derived from height variations by applying a factor 3, i.e.,  $\Delta\phi = (1 - \phi) 3 \frac{\Delta h}{h_0}$  (see text). Porosity decrease at  $t_0$  corresponds to irreversible deformation inherited from sample setup and application of initial  $P_{\text{eff}}$ . Fitting the compaction curve (dashed line) yields a coefficient  $\Delta\phi = 2\%$  for a variation of  $P_{\text{eff}}$  of 1 MPa, which can be roughly converted into  $\Delta\phi = 2\%/100\text{m}$ . Natural compaction curves in Site C0006, either from linear trend in the depth range 50–250 mbsf (porosity from MAD measurement) [Expedition 316 Scientists, 2009a] or from the tangent at 220 mbsf (porosity from resistivity data) [Tobin et al., 2009b], yields a porosity decrease of the order of  $\Delta\phi = 4\%/100\text{m}$  (b) Associated velocity increase during compaction, which can be estimated as  $\Delta V_p \approx 6.10^{-2} \text{ km/s}$  for  $\Delta P_{\text{eff}} = 1 \text{ MPa}$ . Combining porosity and velocity variations trends yields the experimental  $V_p$  versus  $\phi$  relation as  $\Delta V_p = 3 \cdot 10^{-2} \text{ km/s}/\%$ , comparable to the in situ  $V_p$  versus  $\phi$  shown in Figure 12.

factors and that diagenesis and cementation play a minor role, at least in the shallow domain considered here.

### 5.2.1.2. Relative Contribution of Porosity and $P_{\text{eff}}$ Variations to $V_p$

[53] Within mechanical factors, one can distinguish the effect of effective pressure increase and porosity decrease, which both result in an increase in grain-to-grain contact hence on velocity increase. In  $V_p$  versus  $\phi$  empirical relationships such as Figure 13, the two effects cannot be easily differentiated, as low porosity samples generally correspond to larger depths/higher  $P_{\text{eff}}^{\text{in-situ}}$  than high-porosity ones.

[54] On the contrary, in our experiments, during the poroelastic phase, we can directly assess the sole effect of  $P_{\text{eff}}$  on  $V_p$ , as porosity variations are in general of an order of magnitude smaller than  $V_p$  variations. In such cases, the material stiffening due to  $P_{\text{eff}}$  increase may be related to the closure of crack-shaped microcavities or intergrain contacts [e.g., Brace et al., 1972], which hardly affects the

total pore volume, but strongly influences the elastic moduli and hence  $P$  wave velocity.

[55] During the poroelastic deformation of our samples, the effect of  $P_{\text{eff}}$  increase up to 10 MPa is limited to  $\sim 0.25 \text{ km/s}$ . On the other hand, on the  $V_p$  versus  $\phi$  relationships shown in Figure 12 (where in all the samples  $P_{\text{eff}}^{\text{in-situ}}$  was smaller than 10 MPa),  $V_p$  variations are as large as  $\sim 1.2 \text{ km/s}$ . This shows that porosity variations are the primary contribution to  $V_p$  increase and  $P_{\text{eff}}$  only a secondary factor, similarly to the conclusion reached by Erickson and Jarrard [1998] on the basis on multifactor cross-correlation statistical analysis.

### 5.2.2. Mechanical Poroelastic Model in the 30%–60% Porosity Range and Sensitivity of $V_p$ to Material Stiffening

#### 5.2.2.1. Poroelastic Moduli

[56] When considering the three typical end-members described in section 4.1.3, in sample C0007D-17R (limited irreversible compaction) uniaxial compliance is  $-0.0012 \text{ MPa}^{-1}$ , in C0001H-



5H (large irreversible compaction, presence of cement) it is twice that value,  $\sim 0.0022 \text{ MPa}^{-1}$ , while in sample C0007C-8X (large irreversible compaction, no cement) it is  $\sim 0.012 \text{ MPa}^{-1}$ , i.e., ten times larger than in C0007D-17R. Over the range of tested samples, while poroelastic coefficients are affected by very large variations (by a factor of the order of 10), the associated variations in  $P$  wave velocities are limited to  $\sim 50\%$  (Figure 12).

[57] An explanation may be found when regarding the respective values of the distinct terms involved in the  $V_p$  expression

$$V_p = \sqrt{\frac{K_{\text{sat}} + 4/3\mu_{\text{sat}}}{\rho}}$$

Recalling *Gassmann's* [1951] equations for near-incompressible solid grains, the saturated (“undrained”) incompressibility  $K_{\text{sat}}$  is given by

$$K_{\text{sat}} = K_{\text{dry}} + \frac{K_f}{\phi},$$

where  $K_f$  is of the order of 2–3 GPa [*Knauss*, 2005],  $\phi$  the order of 0.5, so that  $\frac{K_f}{\phi}$  is of the order of 4–6 GPa.

[58] In contrast, our measurements of uniaxial compliance are in the range  $-0.01 \sim -0.0012 \text{ MPa}^{-1}$ , which, when converted into “dry” framework incompressibility ( $K_{\text{dry}}^{-1} = -\frac{1}{V_0} \frac{\partial V}{\partial P_{\text{eff}}} = -\frac{3}{h_0} \frac{\partial h}{\partial P_{\text{eff}}}$ , see section 3.3.2), yields  $K_{\text{dry}}$  in the range 30–300 MPa, which is in agreement with modulus estimated from pore fluid variations for isotropic  $P_{\text{eff}}$  loading by *Bourlange et al.* [2004]. Similarly,  $K_{\text{dry}}$  derived from uniaxial consolidation of clays and fine sand by *Karig and Hou* [1992] is at most  $\sim 500 \text{ MPa}$  for porosities down to 25%.

[59] Furthermore, such  $K_{\text{dry}}$  values, determined from drained static experiments are also in agreement with the “dynamic”  $K_{\text{dry}}$  determined from the knowledge of  $V_p$ ,  $V_s$  and  $\rho$  in natural samples [see *Hamilton*, 1971b, Figure 2], within 30%–50% porosity range, where  $K_{\text{dry}}$  is plotted under the label “frame bulk modulus”). These low incompressibilities measured in natural samples stand slightly at variance with the much higher moduli estimated by effective modeling in the high-porosity domain by *Dvorkin et al.* [1999b].

### 5.2.2.2. Mechanical Model of High-Porosity (30%–60%) Sediments

[60] In the limit of very small  $K_{\text{dry}}$  (assuming incompressible solid grains) and null shear modulus, the Gassmann formulation of  $K_{\text{sat}}$  becomes similar

to the simpler suspension model of *Wood* [1941], as they both converge toward  $\frac{K_f}{\phi}$  [e.g., *Wilkins et al.*, 1992] (see Figure 12, where *Wood's* [1941] relationship was calculated for  $K_f(50 \text{ MPa}) = 2.47 \text{ GPa}$ ) [*Knauss*, 2005].

[61] Our experimental  $V_p$ , as well as *Erickson and Jarrard's* [1998] relationship, are faster for a given porosity than *Wood's* [1941] relationship, with a difference that expresses the contribution of solid framework incompressibility  $K_{\text{dry}}$  as well as shear modulus  $\mu_{\text{sat}}$ . The ratio of actual  $V_p$  over  $V_p$  from the suspension model is of the order of 1.1 to 1.2, which implies that the combined contribution of  $K_{\text{dry}}$  and  $\mu_{\text{sat}}$  is of the order of 20%–40% of  $\frac{K_f}{\phi}$ . As the latter term is in the range 4–6 GPa,  $K_{\text{dry}}$  measured in this study accounts only for at most  $\sim 10\%$  of  $\frac{K_f}{\phi}$ . This implies that the shear modulus  $\mu_{\text{sat}}$ , even in the high range (50%–60%) of the tested porosity, is significant, with values of a few hundreds of MPa, i.e., larger than the framework incompressibility.

[62] This conclusion is consistent with logging-derived  $V_s$  for Site 1173 in the range 0.35–0.55 km/s [*Goldberg*, 2003], which convert into values of the shear modulus ( $V_s = \sqrt{\frac{\mu_{\text{sat}}}{\rho}}$ ) of several hundreds of MPa. Similarly, shear modulus estimated from  $V_s$  measurements in experimentally consolidated samples is of the same order even for porosities as large as 50%–60% [*Gettemy and Tobin*, 2003].

[63] In conclusion, in the porosity range of our whole sample set (30%–60%),  $\frac{K_f}{\phi}$  is the controlling factor of  $K_{\text{sat}}$ , as was also stressed out by *Erickson and Jarrard* [1998], with only second-order contributions by the solid framework shear modulus ( $\mu_{\text{sat}}$ ) and third-order contribution by solid framework incompressibility ( $K_{\text{dry}}$ ). One consequence of this low values of  $K_{\text{dry}}$  and  $\mu_{\text{sat}}$  is that  $V_p$  variations reflect mostly the variations in porosity  $\phi$  rather than variations in  $K_{\text{dry}}$  or  $\mu_{\text{sat}}$ , which explains the absence of a clear dependence on lithology (see section 5.1.2 and Figure 12). This principal dependence of  $V_p$  on  $\phi$  results in the fact that the largest errors when interpreting  $V_p$  data originate from uncertainties in the determination of in situ porosity, originating from two main factors: (1) a fraction of measured pore water of the sample (up to 40% of total content) does not correspond to pore space, but to smectite interlayers and is released during drying for porosity measurement [*Brown and Ransom*, 1996], and (2) the amount of elastic rebound, which is required to convert atmospheric pressure measurement of porosity to in situ value, is really ill-constrained (see the large



variations between the three samples in Figure 6, and discussion by *Karig* [1993]).

### 5.2.3. Detection by $V_p$ of Incipient Cementation

#### 5.2.3.1. Test Material: Upper Shikoku Basin From Site 1173

[64] The development of grain-to-grain bonding leads to a significant strengthening, of which one consequence is delayed compaction (underconsolidation), characterized by a porosity larger than average for a given depth [*Leroueil and Vaughan*, 1990], as long as the pore volume is not fully filled with authigenic precipitates. Accordingly, the large porosity of the lower section of the Upper Shikoku Basin (USB) measured in Site 1173 was interpreted as the result of cementation [*Shipboard Scientific Party*, 2001], which was also supported by the observation of a silica phase coating grain contacts as well as the relative evolution of  $V_p$  and  $\phi$  with depth [*Spinelli et al.*, 2007]. Other observations of diagenetic alteration include the progressive illitization of the finer-grained, smectite-rich portions of the USB facies [*Sunderland and Morgan*, 2004]. Both transformations reactions have been related to elevated temperatures in the area of Cape Muroto. As a result of these observations, sediments from the lower section of the USB can be considered as appropriate material in which the mechanical and acoustic effects of cementation can be experimentally characterized.

#### 5.2.3.2. First Indicator: Detection of Cement Destruction

[65] The first experimental evidences of cementation can paradoxically be found when artificially triggering cement destruction, by applying an effective pressure sufficiently large for compaction to resume. In the cemented samples of the USB facies of Site 1173 (254 and 309 mbsf), the state after compaction is characterized by increase, with respect to initial state, in both mechanical compliance  $\frac{1}{h_0} \frac{\partial h}{\partial P_{\text{eff}}}$  and velocity sensitivity on effective pressure  $\frac{\partial V_p}{\partial P_{\text{eff}}}$  (Figure 14a and 14b, right), which may be interpreted as reflecting destruction of intergrain bonds upon compaction onset. It contrasts with the behavior of uncemented samples, where the slopes  $\frac{1}{h_0} \frac{\partial h}{\partial P_{\text{eff}}}$  and  $\frac{\partial V_p}{\partial P_{\text{eff}}}$  in the poroelastic domains are similar before and after compaction (Figure 14b, left).

#### 5.2.3.3. Second Indicator: Low Value of $\frac{\partial V_p}{\partial P_{\text{eff}}}$

[66] In contrast to deeper samples, the cemented samples of USB show a sharp difference in acoustic properties, with a very low dependence of seismic velocity on effective pressure (see Figure 14a, left, and discussion by *Karig* [1993]). This observation may result from the influence of microcracks, shear bands, or microporosity at intergrain contacts. In uncemented samples, such microvoids close upon increase in  $P_{\text{eff}}$ , resulting in material stiffening, hence  $V_p$  increase, while in cemented samples the microvoids may be totally or partially filled by authigenic cement, so that  $V_p$  is much less affected by  $P_{\text{eff}}$  variations. The advantage of the acoustic signature of cementation lies in the fact that  $V_p$  dependence on  $P_{\text{eff}}$  appears relatively constant or, at least, uncorrelated with depth or lithology (Figure 7b). Consequently, the presence of cement can be directly diagnosed from low  $\frac{\partial V_p}{\partial P_{\text{eff}}}$ . In contrast, poroelastic moduli, which can help detecting the presence of cement through material stiffening [*Burland*, 1990; *Karig and Hou*, 1992; *Karig and Ask*, 2003], are quite equivocal indicators as they are also controlled by several other parameters such as porosity, lithological composition or  $P_{\text{eff}}^{\text{in-situ}}$ . As a result, the presence of cement in USB is difficult to infer directly from the compliance profile (Figure 3).

## 5.3. Mechanical State of Material in Nankai Trough

### 5.3.1. Anisotropy

[67] The review of available data for accretionary prism samples does not give a clear picture of  $P$  wave velocity anisotropy pattern. In Nankai, *Bray and Karig* [1986] reported a very low degree of anisotropy of  $V_p$  (measured at atmospheric pressure) in DSDP samples from Sites 582 (hemipelagic mudstones for USB below the trench fill sediments) and 583 (trench fill sediments above the frontal thrust). In contrast,  $V_p$  (measured at atmospheric pressure) in sediments from ODP Site 808 (outer marginal trench wedge to USB and LSB, between 400 and 950 mbsf) is lower in the vertical (i.e., core parallel) direction than in the horizontal direction (irrespective of azimuth) by up to  $\sim 10\%$  [*Brückmann et al.*, 1993]. In accreted sediments within the Barbados accretionary complex, *Brückmann et al.* [1997] reported either positive anisotropy (i.e., horizontal  $V_p$  faster than vertical

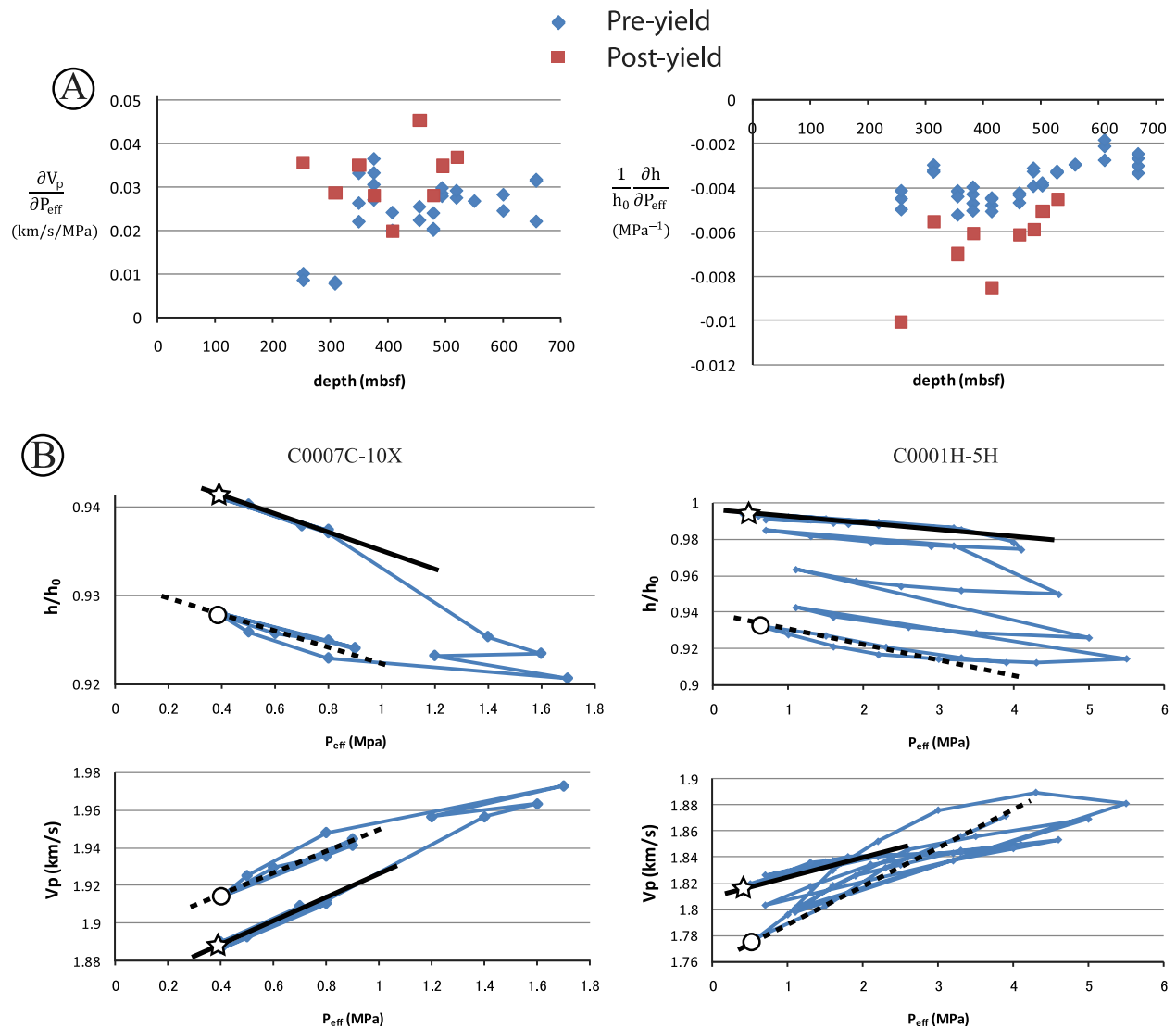


**Figure 14.** (a) Properties  $\frac{1}{h_0} \frac{\partial h}{\partial P_{eff}}$  and  $\frac{\partial V_p}{\partial P_{eff}}$  in samples from Site 1173 before (diamonds) and after (squares) the application of a large  $P_{eff}$ , of the order of  $2P_{eff}^{in-situ}$ . The largest increase (in absolute value) of both mechanical parameters is observed for the two shallowest samples, which are located within the opal-CT cement zone defined by *Spinelli et al.* [2007]. This particular evolution may be interpreted as the breakage of cement bonds during compaction and constitute by consequence a possible indicator of the presence of incipient cementation. (b) Variations in mechanical/acoustic properties before and after irreversible shrinkage. Star (circle) stands for the state at the beginning (end) of the experiment, the solid (dashed) line indicating the associated slopes  $\frac{1}{h_0} \frac{\partial h}{\partial P_{eff}}$  and  $\frac{\partial V_p}{\partial P_{eff}}$ . In sample C0007C-10X, in spite of considerable shrinkage, no significant variation in the slopes is observed, while in sample C0001H-5H, compaction results in a large increase in the modulus of the slopes, i.e., the material becomes more compressible and sensitive to  $P_{eff}$  variations.

one), mostly between 0% and +4%, in hole 948C or no anisotropy in hole 949B (both claystone with total clay content mostly around or above 60%) [Underwood and Deng, 1997], without a clear explanation for the difference between the two sites.

[68] Beside these results on accretionary prisms, the analysis of a larger data set of velocities in silt-clays

sediments and sedimentary rocks from various settings shows that  $V_p$  are statistically lower in vertical than horizontal direction [Bachman, 1979], with an anisotropy calculated with the regression equation that increases with velocity and is in the range 0%–5% for velocities below 3 km/s. This general pattern, determined from atmospheric pressure  $V_p$  measurements, contrasts with the overall very small



anisotropy of  $P$  wave velocity we measured for in situ conditions in our samples (Figure 9a).

[69] One factor influencing anisotropy is the deposition mode: in fine-grained sediments from the Mississippi fan (DSDP leg 96), vertical to horizontal anisotropy is very limited in current-deposited sediments but larger in normally settled, hemipelagic sediments [Wetzel, 1987]. Anisotropy also increases as a result of compaction [Wetzel, 1986]. These trends show that the geometry of the pores and grain-to-grain contacts is essential to anisotropy, which should therefore be also dependent on effective pressure. This effect can somehow explain the discrepancy between atmospheric pressure ( $V_p$  vertical significantly lower than  $V_p$  horizontal) and in situ measurements (very small difference): when effective pressure is applied, some of the intergrain voids close and the velocity increases. This increase is not necessarily the same in the vertical and horizontal directions. Indeed, assuming that lower velocity (for atmospheric pressure measurement) of the vertical direction results from the preferred normal orientation of cracks and micropores, it may be affected, upon  $P_{\text{eff}}$  application, by a velocity increase larger than the horizontal direction, which seems confirmed by our measurements of  $\frac{\partial V_p}{\partial P_{\text{eff}}}$  in the two orthogonal directions (Figure 9b). In other words, lower vertical velocity (for atmospheric pressure measurement) implies, because of preferred orientation of micropores, larger increase upon  $P_{\text{eff}}$  application, so that significant velocity anisotropy measured at atmospheric pressure nearly vanishes for in situ conditions. This result indicates that anisotropy determined at atmospheric pressure may be overestimated with respect to in situ conditions.

### 5.3.2. Mechanical State

#### 5.3.2.1. Weak, Unlithified Shallow Material in Sites C0006 and C0007

[70] Although consolidation studies usually focused on the yield point, i.e., the effective stress for which plastic deformation resumes [Feeser *et al.*, 1993; Moran *et al.*, 1993; Morgan and Ask, 2004; Vrolijk *et al.*, 1998], there has been little attention paid to the volume shrinkage when very low stresses, much below yield, are applied, either during resaturation of the sample or during the first steps of the test itself. This deformation was significant only for shallow material in Sites C0006 (samples 20X, 25X, 30X, 35X) and 7 (8X and 10X), i.e., for

trench facies sediments, which have a lower clay fraction than other tested samples.

[71] As the shrinkage occurs for an effective pressure much lower than  $P_{\text{eff}}^{\text{in-situ}}$ , in situ sample volume must incorporate this shrinkage, which implies that there was a significant volume expansion in the time lapse between coring and the start of our experiments. Such expansion is some sort of porosity rebound, although the reference curves by Hamilton [1976] show an amount of rebound that increases with depth, i.e., deep samples should be affected by a larger amount of expansion/shrinkage than shallower ones, which is not the case here. It should be noted that the porosity rebound is calculated on the basis of consolidation curves upon pressure release [Lee, 1973; Silva and Hollister, 1973]. On the other hand, the volume shrinkage in our samples was not reversible upon pressure release. This implies that, compared to porosity rebound, which is an immediate and elastic process, the volume expansion affecting our samples is slower. Time-dependent anelastic strain recovery measured in samples from C0002 and C0006 is by a few orders smaller than the volume variations described here [Byrne *et al.*, 2009], but their samples correspond to large depths, where we did not observe any significant sample shrinkage. Independently of the precise mechanism at stake and its timing, this volume shrinkage, which is not correlated with changes in lithology or age gap, attest to the low mechanical cohesion of the affected samples and unravels the presence of a mechanical boundary in Sites C0006 and 7 in the depths range (250–350 mbsf) and (100–300 mbsf), respectively.

#### 5.3.2.2. Cemented Material in Sites 1173 and C0001

[72] We observed a large increase in both poroelastic compliance and  $\frac{\partial V_p}{\partial P_{\text{eff}}}$  after plastic deformation in samples C0001H-5R, C0001H-12R and C0001H-16R, a behavior very similar to the samples of USB of Site 1173 where the deformation led to cement destruction (see section 5.2.3 and Figure 14b). Such behavior is not observed in other deformable samples, such as C0007C-10, where acoustic and poroelastic moduli are left roughly unchanged by the volume shrinkage.

[73] In addition, our samples from Site C0001 are characterized by a very low  $\frac{\partial V_p}{\partial P_{\text{eff}}}$ , which is also observed in cemented samples from USB. Finally, as a third common attribute, samples from Site C0001 share the same response to consolidation as USB: little deformation down to a critical value of



$P_{\text{eff}}$  close to the calculated  $P_{\text{eff}}^{\text{in-situ}}$ , then for larger  $P_{\text{eff}}$  a very large plastic shrinkage.

[74] All these attributes indirectly support the presence of rock-strengthening cement in C0001 (accretionary prism unit). As this unit is probably the proximal equivalent of the USB cored along the Muroto transect [Expedition 315 Scientists, 2009b], the cementing agent may be similar, either authigenic opal [Spinelli et al., 2007] or clay [Ujue et al., 2003], though our mechanical tests provide no evidence as regards the nature of the cement.

## 5.4. Critical Porosity

### 5.4.1. In Terms of $V_p$ Evolution

[75] The concept of critical porosity ( $\phi_{\text{critical}}$ ) is defined as transition from a fluid-supported to a matrix-supported state [Dvorkin et al., 1999b; Nur et al., 1998]. In such model, in the high-porosity regime ( $\phi > \phi_{\text{critical}}$ ), the sediment behave like a suspension, i.e., without rigidity and with incompressibility modulus given by Wood's [1941] equations. It is not completely appropriate, as (1) high-porosity sediment  $V_p$  are faster than predicted in the suspension model (Figure 12) [Hamilton, 1971b], (2) they have a small but nonnegligible "dry" framework incompressibility  $K_{\text{dry}}$  (Figure 3), and (3) they can transmit shear waves, i.e., they have nonnull rigidity [e.g., Hamilton et al., 1970], which shows that there is a solid particle framework with some strength, even at very high porosity. Because of these shortcomings, in a modified version of the model [e.g., Erickson and Jarrard, 1998], the critical porosity corresponds simply to the sharp increase in the solid framework strength around some porosity, reflected in a sharp increase in  $V_p$ . The precise value of this critical porosity is not clearly defined: the value of ~40% is given for sandstones by Nur et al. [1998], while  $\phi_{\text{critical}}$  is in the range 27%–40% for arenites [Vernik, 1998]. For a wider range of sediments, including shales, the critical porosity defined by Erickson and Jarrard [1998] is either 0.31 or 0.39, depending on the degree of consolidation and irrespectively of the lithology, while for Hoffman and Tobin [2004], for various trench facies and hemipelagic sediments from the Nankai Trough,  $\phi_{\text{critical}}$  is estimated as 0.295. On the other hand, for clay-supported siliciclastics, Vernik [1998] proposes that on the contrary to grain-supported material, no sharp transition in strength

around a given porosity, i.e., no critical porosity, exists.

[76] As Erickson and Jarrard [1998] and Hoffman and Tobin [2004] approaches are empirical and based on curve-fitting, it is not sure whether a critical porosity, i.e., sharp increase in  $V_p$  around a given value of the porosity, is actually present or not. Moreover, as the transition from fluid- to matrix-supported state is not a valid model, the physical meaning of the critical porosity is unclear.

[77] As our samples encompass a porosity range over 30%  $\phi_{\text{critical}}$ , we cannot rule out the possibility of a sharp increase in material strength around some critical value of the porosity below 30%. Nevertheless, the definition of  $\phi_{\text{critical}}$  in terms of  $V_p$ , and not poroelastic moduli, introduces a bias, inasmuch as for our high-porosity (30%–60%) material, the tenfold increase in framework incompressibility  $K_{\text{dry}}$  (Figure 3) is hardly reflected in  $V_p$ , which is principally controlled by water incompressibility. As a consequence, the sharp increase in  $V_p$  that may define  $\phi_{\text{critical}}$  reflects the point where the strength of the framework becomes of the same order as the fluid strength, while the increase in framework strength occurs actually over a much larger porosity range, for porosity above  $\phi_{\text{critical}}$ .

[78] In addition, clays and sand prepared from disaggregated particles that were experimentally consolidated down to large  $P_{\text{eff}}$  (~20 MPa) by Karig and Hou [1992] have still relatively low poroelastic moduli (Young's modulus  $E \leq 1$  GPa) with respect to fluid strength, even when porosities reach very low values. (~25% for sand and 20% for clays). In contrast, natural samples of equivalent lithology and porosity have moduli 10 times larger, reflected in much higher  $P$  wave velocities. This shows that rather than porosity, the major control in the sharp increase in  $V_p$  for intermediate- to low-porosity sediments is cement. The physical meaning, in terms of poroelastic strength, of the critical porosity, appears therefore questionable, especially in clay-rich material such as the one studied here.

### 5.4.2. In Terms of Consolidation

[79] While the idea of the critical porosity has been much exploited in determining the relationship between  $V_p$  and  $\phi$ , its consequences for consolidation have not been explored. In their physical model, Nur et al. [1998] define the critical porosity as corresponding to a compact arrangement of



particles, theoretically around 36% for rigid spheres of a given diameter. If such compact state is relevant, compaction processes above and below such a porosity threshold are fundamentally different: above the critical porosity ( $\phi > \phi_{\text{critical}}$ ), sliding at grain-to-grain interfaces enables their redistribution and global porosity reduction, while below ( $\phi < \phi_{\text{critical}}$ ), a change in the grain shape itself (from grain fracturing or pressure solution, for example) is required to sustain the porosity reduction. As a result, rates of consolidation should be different in the two domains of porosity.

[80] Our results seem to support these two distinct behavior: in Sites 1173 and C0006, upon application of a large  $P_{\text{eff}}$ , in the range 1.5–2.5  $P_{\text{eff}}^{\text{in-situ}}$  (Figure 5b and 5c), there is a relatively sharp transition from shallower samples with a large irreversible shrinkage to deeper ones, where the shrinkage is limited. Semiquantitative XRD analysis of the material (Figure 5d) attests that mineralogy is relatively homogeneous (except for the two deep samples of C0006 pertaining to a different unit) and cannot account for such large differences.

[81] The case of Site 1173 is complicated, as the depth distribution of cement [Spinelli et al., 2007; Sunderland and Morgan, 2004; Ujiie et al., 2003] has a large impact on the mechanical state. On the other hand, in Site C0006, where no evidence for cement was found, porosity is probably the best candidate for the material response to consolidation. The value of the porosity for the transition in mechanical behavior is 38%–42% at Site C0006 (Figure 5, top, horizontal gray band), in good agreement with the value of 40% given by Nur et al. [1998] for the critical porosity in sandstones, even if our material is richer in clay. The relatively low plastic deformation of low-porosity samples can be explained if they are in compact state and if applied stresses were too low to trigger grain cataclasis and experiment duration too small for chemical transport to be efficient. Hence, experimental compaction of samples with  $\phi < \phi_{\text{critical}}$  may be inhibited, or at least very limited in comparison with samples with  $\phi > \phi_{\text{critical}}$ .

[82] Nevertheless literature data on consolidation does not evoke this idea of critical porosity influencing consolidation. For example, profiles of porosity versus depth are usually fitted by a unique law, either exponential [Athy, 1930] or polynomial [Hamilton, 1976], i.e., the existence of two domains of porosity, with distinct consolidation behavior, is not considered. Second, in geotechnical testing, no

mention is made of a critical porosity separating two domains of behavior.

[83] In consolidation tests, deformation is often represented by a compressibility factor, which relates the void ratio or the porosity to the log of the effective stress. Between poroelastic deformation and primary consolidation (i.e.,  $\frac{\partial \phi}{\partial P_{\text{eff}}}$  similar to in situ conditions), Karig and Ask [2003] define a tertiary consolidation, proper to laboratory high rates of loading, where the plastic deformation occurs with much lower compressibility than primary consolidation phase. This tertiary consolidation is probably what occurs in our deep samples, where the experimental deformation is really limited. In line with the concept of critical porosity, one may wonder whether such low compressibility tertiary consolidation is associated only with low-porosity samples. In the work by Karig and Ask [2003], tertiary consolidation is described for samples with porosity in the range 30%–40%. In the study by Karig [1996], low compressibility consolidation occurs for samples with porosity in the range 30%–35%. In the study by Morgan and Ask [2004], where largest porosity is ~45%, applied effective stress must be increased to a much higher value than yield stress for a significant deformation to occur, i.e., for effective stresses up to twice in situ effective value (assuming hydrostatic condition), the plastic deformation is very limited. In the study by Feeser et al. [1993], the two deeper samples (porosity in the range 35%–50%) [Shipboard Scientific Party, 1991b] did not reach primary consolidation and were affected by very little deformation, on the contrary to the shallow samples (porosity in the range 50%–65%). These results support the occurrence of tertiary consolidation with low compressibility, hence limited total deformation, only in deep, low-porosity samples, while shallow samples seem to reach primary consolidation, with larger compressibility, without undergoing this phase. If this explanation may explain the variable deformation between shallow and deep samples observed in our samples, it is nevertheless not clear at all whether such transition is associated with critical porosity.

## 6. Conclusions

[84] The four parameters concomitantly estimated during our experiments ( $V_p$ , uniaxial poroelastic compliance  $\frac{1}{h_0} \frac{\partial h}{\partial P_{\text{eff}}}$ , sensitivity of  $V_p$  to effective pressure  $\frac{\partial V_p}{\partial P_{\text{eff}}}$ , irreversible shrinkage upon application of a large effective pressure) yielded comple-



mentary insights on the state of the various samples tested in the Nankai Trough subduction zone (250–1000 mbsf depth range, hemipelagic to trench facies). The main findings can be summarized as follows.

[85] 1. Evidence for incipient cementation is detected by its experimental destruction when compactional force is imposed, which leads to a large increase in compliance and  $V_p$  sensitivity to  $P_{\text{eff}}$ , as well as low  $\frac{\partial V_p}{\partial P_{\text{eff}}}$ . On the basis of such attributes, we inferred the presence of cement in Site C0001 (accretionary prism unit) in addition to USB in Site 1173.

[86] 2. The amount of irreversible shrinkage varies strongly through the samples (Figure 4), leading to identify a low porosity domain with limited irreversible deformation and a high-porosity domain where large mechanical compaction occurred. While it is not clear whether such mechanical transition can be related to some critical value of the porosity, the change in response seems to occur around 3–4 MPa effective confining stress.

[87] 3. Poroelastic moduli increase continuously and by a large magnitude upon porosity decrease (Figure 3), which is generally not reflected by the subtle, low-magnitude  $V_p$  variations (Figure 12).

[88] The latter point, as well as the slight discrepancy between core/log and seismic velocities, point out the need for further experimental calibration of the relationships between acoustic attributes and physical properties, in particular when extrapolated to larger depths via seismic reflection profiling

## Appendix A

[89] The porosity of the core samples we used in our experiments was determined on trimmings from sample preparation, measuring its relative loss of weight after drying at 105°C overnight and converting it to porosity by using the value for grain density of the closest sample measured on board (MAD measurements, see Table 1). Then we applied on this porosity a correction to restore in situ conditions, calculated from monitored values of  $\frac{\Delta h}{h_0}$  as a range comprised between two extreme cases, either no radial deformation ( $\frac{\partial V_{\text{fluid}}}{V_{\text{total}}} = \frac{\Delta h}{h_0}$ ) or isotropic deformation ( $\frac{\partial V_{\text{fluid}}}{V_{\text{total}}} = 3\frac{\Delta h}{h_0}$ ). This correction for rebound is extremely variable between samples (as visible in the size of the range of the porosity correction in Figure 12), making it difficult to derive general porosity rebound laws such as in the work by *Hamilton* [1976].

[90] In situ porosity for logging data is derived from resistivity, smoothed by averaging over 20 m thick depth interval, as this is the only physical measurement available for all the holes surveyed by Expedition 314 (Sites C0001, C0002, and C0006). The relatively good agreement (Figure A1) between resistivity-derived porosity and our in situ, laboratory-derived core porosity (with rebound correction) allows for comparison between the different data sets, although in detail there are often slight discrepancies, such as logging porosity either lower (up to ~5% of porosity) for Site C0001 and higher for Site C0002 (up to ~5% of porosity).

[91] On Figure A1 is also plotted another measurement of porosity, derived from bulk density logging, which is also in good agreement with our laboratory-derived core porosity (with rebound correction). This enables the comparison done in Figure 12 between our core/logging data with *Erickson and Jarrard* [1998] and *Hoffman and Tobin* [2004]  $V_p$  versus  $\phi$  relationships, where in both cases porosity was derived from density logs.

[92] Please note also that we do not apply any correction for the water bounded to clay [*Conin et al.*, 2011]. This bounded water significantly affects the porosity of our samples estimated by MAD measurements, but as the density-derived porosity used by *Erickson and Jarrard* [1998] and *Hoffman and Tobin* [2004] is calculated with a solid grain density also estimated by MAD measurements, for the consistency of our data with theirs we did not correct for the bounded water. Finally, as the correction for clay content to be applied to resistivity-derived porosity is of the same order as the one to MAD porosity [*Conin et al.*, 2011], we use for the logging data (C0001, C0002, C0004 and C0006) in Figure 12 resistivity-derived porosity uncorrected for the clay content, for a similar reason of data set consistency. The consequence is that the porosity plotted in Figure 12 may be a bit higher than “true” interstitial porosity, but all the data sets are inter-comparable.

## Appendix B

[93] If one tries to determine to which extent a given error on velocity affects the other properties, using *Hoffman and Tobin*'s [2004] relationship, a difference in  $V_p$  from 2 to 2.1 km/s leads to a porosity difference of ~0.03, from 0.357 to 0.327. These two porosities, when expressed as void ratio  $\phi/(1 - \phi)$  (yielding 0.555 and 0.486, respectively), can be converted into effective stresses using field-

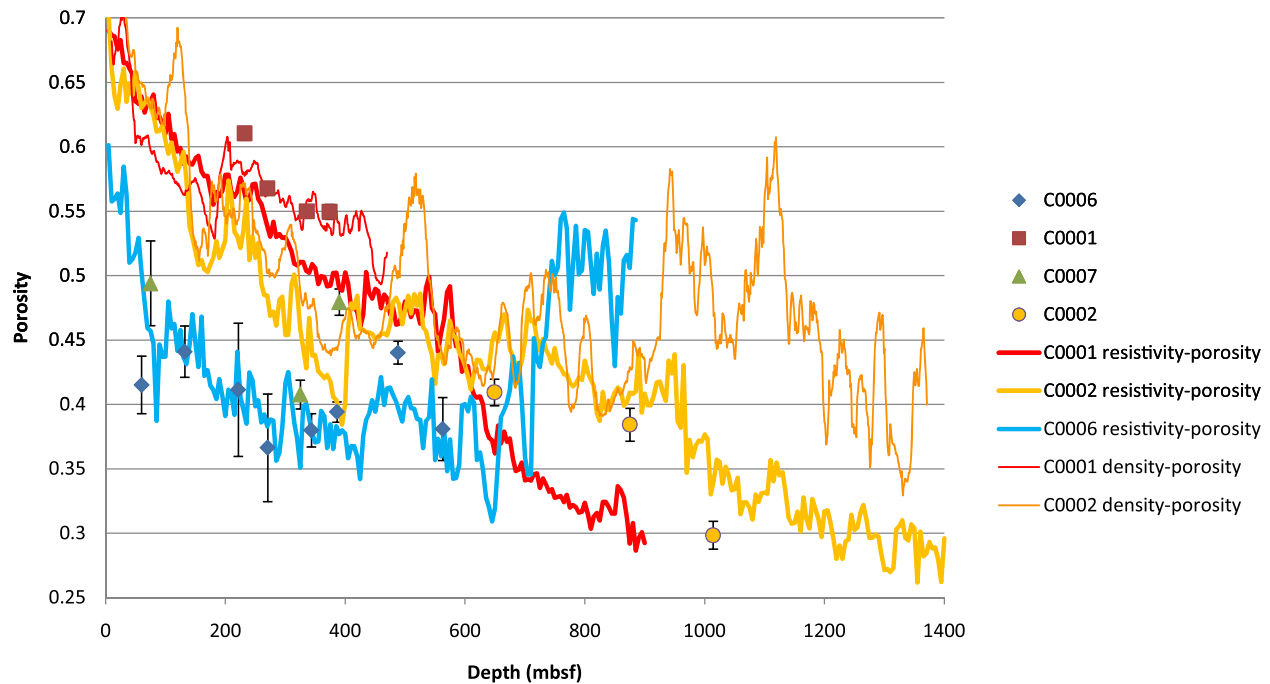


**Figure A1.** Comparison of (1) MAD measurements of the porosity of the core samples used in our experiments (with correction for rebound; see text) and (2) porosity derived from logging data, either resistivity or bulk density [Expedition 314 Scientists, 2009].

based virgin consolidation curves in the work by Saffer [2003]. As a result, the equilibrium stress corresponding to  $V_p = 2$  km/s is 5.1 MPa, while for  $V_p = 2.1$  km/s, stress is 5.7 MPa, i.e., a difference in velocity as small as 0.1 km/s leads to differences in stresses as large as  $\sim 0.6$  MPa, which are significant with respect to  $P_{\text{eff}}^{\text{in-situ}}$  for the relatively shallow rocks ( $<1000$  mbsf) considered here.

## Acknowledgments

[94] This research used samples and data provided by the Ocean Drilling Program (ODP) and Integrated Ocean Drilling Program (IODP). Support for the project was provided by the Grant-in-Aid for Creative Scientific Research (19GS0211) by MEXT (Ministry of Education, Culture, Sports, Science and Technology) of Japan. We thank the staff in Kochi Core Center for their help with sampling. The paper benefited greatly from the very detailed comments by three anonymous reviewers.

## References

- Athy, L. F. (1930), Density, porosity, and compaction of sedimentary rocks, *AAPG Bull.*, *14*, 1–23.
- Bachman, R. T. (1979), Acoustic anisotropy in marine sediments and sedimentary rocks, *J. Geophys. Res.*, *84*, 7661–7663.
- Bangs, N. L. B., and S. P. S. Gulick (2005), Physical properties along the developing decollement in the Nankai Trough: Inferences from 3-D seismic reflection data inversion and Leg 190 and 196 drilling data, *Proc. Ocean Drill. Program*

*Sci. Results*, *190/196*, 1–18, doi:10.2973/odp.proc.sr.190196.190354.192005.

- Bangs, N. L., et al. (1999), Fluid accumulation and channeling along the northern Barbados Ridge decollement thrust, *J. Geophys. Res.*, *104*, 20,399–20,414.
- Bangs, N. L., et al. (2009), Broad, weak regions of the Nankai megathrust and implications for shallow coseismic slip, *Earth Planet. Sci. Lett.*, *284*, 44–49, doi:10.1016/j.epsl.2009.04.026.
- Best, A. I., et al. (2001), Comparison of in situ and laboratory acoustic measurements on Lough Hyne marine sediments, *J. Acoust. Soc. Am.*, *110*(2), 695–709, doi:10.1121/1.1382616.
- Blum, P. (1997), Physical properties handbook: A guide to the shipboard measurement of physical properties of deep-sea cores, *Tech. Note 26*, Ocean Drill. Program, College Station, Tex. (Available at <http://www-odp.tamu.edu/publications/tnotes/tn26/INDEX.HTM>)
- Bourlange, S., et al. (2004), Data report: Permeability, compressibility, and friction coefficient measurements under confining pressure and strain, Leg 190, Nankai Trough, *Proc. Ocean Drill. Program Sci. Results*, *190/196*, 1–16, doi:10.2973/odp.proc.sr.190196.190215.192004.
- Brace, W. F., et al. (1968), Permeability of granite under high pressure, *J. Geophys. Res.*, *80*, 2225–2236.
- Brace, W. F., et al. (1972), Cracks and pores: A closer look, *Science*, *178*, 162–164, doi:10.1126/science.178.4057.162.
- Bray, C. J., and D. E. Karig (1986), Physical properties of sediments from the Nankai Trough, Deep Sea Drilling Project Leg 87A, Sites 582 and 583, *Initial Rep. Deep Sea Drill. Proj.*, *87*, 827–842. doi:10.2973/dsdp.proc.2987.2128.1986.
- Brown, K. M., and B. Ransom (1996), Porosity corrections for smectite-rich sediments: Impact on studies of compaction, fluid generation, and tectonic history, *Geology*, *24*,



- 843–846, doi:10.1130/0091-7613(1996)024<0843:PCFSRS>2.3.CO;2.
- Brückmann, W., et al. (1993), Acoustic anisotropy and micro-fabric development in accreted sediments from the Nankai Trough, *Proc. Ocean Drill. Program Sci. Results*, *131*, 221–233, doi:10.2973/odp.proc.sr.2131.2121.1993.
- Brückmann, W., et al. (1997), Directional properties of *P* wave velocities and acoustic anisotropy in different structural domains of the northern Barbados Ridge accretionary complex, *Proc. Ocean Drill. Program Sci. Results*, *156*, 115–123, doi:10.2973/odp.proc.sr.2156.2017.1997.
- Burland, J. B. (1990), On the compressibility and shear strength of natural clays, *Geotechnique*, *40*, 329–378, doi:10.1680/geot.1990.40.3.329.
- Byrne, T. B., et al. (2009), Anelastic strain recovery reveals extension across SW Japan subduction zone, *Geophys. Res. Lett.*, *36*, L23310, doi:10.1029/2009GL040749.
- Casagrande, A. (1936), The determination of the pre-consolidation load, *Proc. Int. Conf. Soil Mech. Found. Eng.*, *3*, 60–64.
- Conin, M., et al. (2011), Interpretation of LWD resistivity from Nankai accretionary wedge in the light of clay physico-chemical properties: Evidence for erosion and local overpressuring, *Geochem. Geophys. Geosyst.*, *12*, Q0AD07, doi:10.1029/2010GC003381.
- Dvorkin, J., et al. (1999a), Overpressure detection from compressional- and shear-wave data, *Geophys. Res. Lett.*, *26*, 3417–3420.
- Dvorkin, J., et al. (1999b), Elasticity of marine sediments: Rock physics modeling, *Geophys. Res. Lett.*, *26*, 1781–1784.
- Erickson, S. N., and R. D. Jarrard (1998), Velocity-porosity relationships for water-saturated siliciclastic sediments, *J. Geophys. Res.*, *103*, 30,385–30,406.
- Expedition 314 Scientists (2009), Expedition 314 methods, *Proc. Integr. Ocean Drill. Program*, *314/315/316*, 1–33, doi:10.2204/iodp.proc.314315316.314315112.314312009.
- Expedition 315 Scientists (2009a), Expedition 315 methods, *Proc. Integr. Ocean Drill. Program*, *314/315/316*, 1–57, doi:10.2204/iodp.proc.314315316.314315122.314312009.
- Expedition 315 Scientists (2009b), Expedition 315 Site C0001, *Proc. Integr. Ocean Drill. Program*, *314/315/316*, 1–104, doi:10.2204/iodp.proc.314315316.314315123.314312009.
- Expedition 315 Scientists (2009c), Expedition 315 Site C0002, *Proc. Integr. Ocean Drill. Program*, *314/315/316*, 1–76, doi:10.2204/iodp.proc.314315316.314315124.314312009.
- Expedition 316 Scientists (2009a), Expedition 316 Site C0006, *Proc. Integr. Ocean Drill. Program*, *314/315/316*, 1–124, doi:10.2204/iodp.proc.314315316.314315134.314312009.
- Expedition 316 Scientists (2009b), Expedition 316 Site C0007, *Proc. Integr. Ocean Drill. Program*, *314/315/316*, 1–110, doi:10.2204/iodp.proc.314315316.314315135.314312009.
- Feeser, V., et al. (1993), Stress-regime-controlled yield and strength behavior of sediment from the frontal part of the Nankai accretionary prism, *Proc. Ocean Drill. Program Sci. Results*, *131*, 261–273, doi:10.2973/odp.proc.sr.2131.2123.1993.
- Fofonoff, N. P. (1985), Physical properties of seawater: A new salinity scale and equation of state for seawater, *J. Geophys. Res.*, *90*, 3332–3342.
- Gassmann, F. (1951), Über die Elastizität poroser Medien, *Vierteljahrsschr. Naturforsch. Ges. Zuerich*, *96*, 1–23.
- Gettemy, G. L., and H. J. Tobin (2003), Tectonic signatures in centimeter-scale velocity-porosity relationships of Costa Rica convergent margin sediments, *J. Geophys. Res.*, *108*(B10), 2494, doi:10.1029/2001JB000738.
- Goldberg, D. (2003), Data report: Reprocessing of wireline sonic logs in turbidites and hemipelagic sediments at ODP Site 1173, *Proc. Ocean Drill. Program Sci. Results*, *190/196*, 1–15, doi:10.2973/odp.proc.sr.190196.190209.192003.
- Gorgas, T. J., et al. (2002), In situ acoustic and laboratory ultrasonic sound speed and attenuation measured in heterogeneous soft seabed sediments: Eel River shelf, California, *Mar. Geol.*, *182*, 103–119, doi:10.1016/S0025-3227(01)00230-4.
- Hamilton, E. L. (1971a), Prediction of in situ acoustic and elastic properties of marine sediments, *Geophysics*, *36*(2), 266–284, doi:10.1190/1.1440168.
- Hamilton, E. L. (1971b), Elastic properties of marine sediments, *J. Geophys. Res.*, *76*, 579–604.
- Hamilton, E. L. (1976), Variations of density and porosity with depth in deep-sea sediments, *J. Sediment. Petrol.*, *46*(2), 280–300.
- Hamilton, E. L., et al. (1970), Velocities of compressional and shear waves in marine sediments determined in situ from a research submersible, *J. Geophys. Res.*, *75*, 4039–4049.
- Hoffman, N. W., and H. J. Tobin (2004), An empirical relationship between velocity and porosity for underthrust sediments in the Nankai Trough accretionary prism, *Proc. Ocean Drill. Program Sci. Results*, *190/196*, 1–23, doi:10.2973/odp.proc.sr.190196.190355.192004.
- Hyndman, R. D., et al. (1993), Velocity, porosity, and pore-fluid loss from the Nankai subduction zone accretionary prism, *Proc. Ocean Drill. Program Sci. Results*, *131*, 211–220, doi:10.2973/odp.proc.sr.2131.2125.1993.
- Johns, M. W. (1986), Consolidation and permeability characteristics of Japan Trench and Nankai Trough sediments from Deep Sea Drilling Project Leg 87, Sites 582, 583 and 584, *Initial Rep. Deep Sea Drill. Proj.*, *87*, 843–849, doi:10.2973/dsdp.proc.2987.2129.1986.
- Karig, D. E. (1993), Reconsolidation tests and sonic velocity measurements of clay-rich sediments from the Nankai Trough, *Proc. Ocean Drill. Program Sci. Results*, *131*, 247–260, doi:10.2973/odp.proc.sr.2131.2127.2199.
- Karig, D. E. (1996), Uniaxial reconsolidation tests on porous sediments: Mudstones from Site 897, *Proc. Ocean Drill. Program Sci. Results*, *149*, 363–373, doi:10.2973/odp.proc.sr.149.234.1996.
- Karig, D. E., and M. V. S. Ask (2003), Geological perspectives on consolidation of clay-rich marine sediments, *J. Geophys. Res.*, *108*(B4), 2197, doi:10.1029/2001JB000652.
- Karig, D. E., and G. Hou (1992), High-stress consolidation experiments and their geologic implications, *J. Geophys. Res.*, *97*, 289–300.
- Kibblewhite, A. C. (1989), Attenuation of sound in marine sediments: A review with emphasis on new low-frequency data, *J. Acoust. Soc. Am.*, *86*(2), 716–738, doi:10.1121/1.398195.
- Knauss, J. A. (2005), *Introduction to Physical Oceanography*, 320 pp., Waveland Press, Long Grove, Ill.
- Lee, H. (1973), Measurements and estimates of engineering and other physical properties, *Initial Rep. Deep Sea Drill. Proj.*, *19*, 701–719, doi:10.2973/dsdp.proc.2919.2122.1973.
- Leroueil, S., and P. R. Vaughan (1990), The general and congruent effects of structure in natural soils and rocks, *Geotechnique*, *40*, 467–488, doi:10.1680/geot.1990.40.3.467.
- Mavko, G., et al. (2009), *The Rock Physics Handbook: Tools for Seismic Analysis in Porous Media*, 2nd ed., Cambridge Univ. Press, Cambridge, U. K., doi:10.1017/CBO9780511626753.



- Moore, G. F., et al. (2005), Legs 190 and 196 synthesis: Deformation and fluid flow processes in the Nankai Trough accretionary prism, *Proc. Ocean Drill. Program Sci. Results, 190/196*, 1–26. doi:10.2973/odp.proc.sr.190196.190201.192005.
- Moore, G. F., et al. (2009), Structural and seismic stratigraphic framework of the NanTroSEIZE Stage 1 transect, *Proc. Integr. Ocean Drill. Program, 314/315/316*, 1–46, doi:10.2204/iodp.proc.314315316.314315102.314312009.
- Moore, J. C., et al. (1995), Abnormal fluid pressures and fault-zone dilation in the Barbados accretionary prism: Evidence from logging while drilling, *Geology*, *23*, 605–608, doi:10.1130/0091-7613(1995)023<0605:AFPAFZ>2.3.CO;2.
- Moran, K., et al. (1993), In situ stress conditions at Nankai Trough, Site 808, *Proc. Ocean Drill. Program Sci. Results, 131*, 283–291, doi:10.2973/odp.proc.sr.2131.2129.1993.
- Morgan, J. K., and M. V. S. Ask (2004), Consolidation state and strength of underthrust sediments and evolution of the décollement at the Nankai accretionary margin: Results of uniaxial reconsolidation experiments, *J. Geophys. Res.*, *109*, B03102, doi:10.1029/2002JB002335.
- Nur, A., et al. (1998), Critical porosity: A key to relating physical properties to porosity in rocks, *Lead. Edge*, *17*, 357–362, doi:10.1190/1.1437977.
- Park, J. O., et al. (2002), A deep strong reflector in the Nankai accretionary wedge from multichannel seismic data: Implications for underplating and interseismic shear stress release, *J. Geophys. Res.*, *107*(B4), 2061, doi:10.1029/2001JB000262.
- Robb, G. B. N., et al. (2007), Measurement of the in situ compressional wave properties of marine sediments, *IEEE J. Oceanic Eng.*, *32*(2), 484–496, doi:10.1109/JOE.2006.880430.
- Saffer, D. M. (2003), Pore pressure development and progressive dewatering in underthrust sediments at the Costa Rican subduction margin: Comparison with northern Barbados and Nankai, *J. Geophys. Res.*, *108*(B5), 2261, doi:10.1029/2002JB001787.
- Saffer, D. M., and B. A. Bekins (1998), Episodic fluid flow in the Nankai accretionary complex: Timescale, geochemistry, flow rates and fluid budget, *J. Geophys. Res.*, *103*, 30,351–30,370.
- Saffer, D. M., and B. A. Bekins (2006), An evaluation of factors influencing pore pressure in accretionary complexes: Implications for taper angle and wedge mechanics, *J. Geophys. Res.*, *111*, B04101, doi:10.1029/2005JB003990.
- Saffer, D., L. McNeill, E. Araki, T. Byrne, N. Eguchi, S. Toczko, and K. Takahashi, and the Expedition 319 Scientists (2009), NanTroSEIZE Stage 2: NanTroSEIZE riser/riserless observatory, *Integr. Ocean Drill. Program Prelim. Rep.*, *319*, doi:10.2204/iodp.pr.319.2009.
- Screaton, E. J., et al. (2002), Porosity loss within the underthrust sediments of the Nankai accretionary complex: Implications for overpressures, *Geology*, *30*, 19–22, doi:10.1130/0091-7613(2002)030<0019:PLWTUS>2.0.CO;2.
- Shipboard Scientific Party (1991a), Geological background and objectives, *Proc. Ocean Drill. Program Initial Rep.*, *131*, 5–14, doi:10.2973/odp.proc.ir.2131.2101.1991.
- Shipboard Scientific Party (1991b), Site 808, *Proc. Ocean Drill. Program Initial Rep.*, *131*, 71–269.
- Shipboard Scientific Party (2001), Site 1173, *Proc. Ocean Drill. Program Initial Rep.*, *190*, 1–147, doi:10.2973/odp.proc.ir.2190.2104.2001.
- Silva, A., and C. D. Hollister (1973), Geotechnical properties of ocean sediments recovered with giant piston corer: 1. Gulf of Maine, *J. Geophys. Res.*, *78*, 3597–3616.
- Spinelli, G., et al. (2007), Diagenesis, sediment strength, and pore collapse in sediment approaching the Nankai Trough subduction zone, *Geol. Soc. Am. Bull.*, *119*(3–4), 377–390, doi:10.1130/B25920.1.
- Steurer, J. F., and M. Underwood (2005), Clay mineralogy of mudstones from the Nankai Trough references Sites 1173 and 1177 and frontal accretionary prism Site 1174, *Proc. Ocean Drill. Program Sci. Results, 190/196*, 1–37, doi:10.2973/odp.proc.sr.190196.190211.192003.
- Sunderland, E. B., and J. K. Morgan (2004), Microstructural variations in sediments from the toe of the Nankai accretionary prism: Results of scanning electron microscope analysis, *Proc. Ocean Drill. Program Sci. Results, 190/196*, 1–27, doi:10.2973/odp.proc.sr.190196.190212.192004.
- Taira, A., et al. (1988), The Shimanto Belt in Shikoku, Japan—Evolution of Cretaceous to Miocene accretionary prism, *Mod. Geol.*, *12*, 5–46.
- Tobin, H. J., and J. C. Moore (1994), Fluid pressure in the frontal thrust of the Oregon accretionary prism: Experimental constraints, *Geology*, *22*, 979–982, doi:10.1130/0091-7613(1994)022<0979:FPITFT>2.3.CO;2.
- Tobin, H. J., and D. M. Saffer (2009), Elevated fluid pressure and extreme mechanical weakness of a plate boundary thrust, Nankai Trough subduction zone, *Geology*, *37*, 679–682, doi:10.1130/G25752A.1.
- Tobin, H., et al. (2009a), NanTroSEIZE Stage 1 expeditions: Introduction and synthesis of key results, *Proc. Integr. Ocean Drill. Program, 314/315/316*, 1–20, doi:10.2204/iodp.proc.314315316.314315101.314312009.
- Tobin, H., et al. (2009b), Expedition 314 summary, *Proc. Integr. Ocean Drill. Program, 314/315/316*, 1–42, doi:10.2204/iodp.proc.314315316.314315111.314312009.
- Ujiie, K., et al. (2003), Deformation and fluid pressure variation during initiation and evolution of the plate boundary décollement zone in the Nankai accretionary prism, *J. Geophys. Res.*, *108*(B8), 2398, doi:10.1029/2002JB002314.
- Underwood, M., and X. Deng (1997), Clay mineralogy and clay geochemistry in the vicinity of the décollement, northern Barbados Ridge, *Proc. Ocean Drill. Program Sci. Results, 156*, 3–30, doi:10.2973/odp.proc.sr.2156.2001.1997.
- Urmos, J., and R. H. Wilkens (1993), In situ velocities in pelagic carbonates: New insights from Ocean Drilling Program Leg 130, Ontong Java Plateau, *J. Geophys. Res.*, *98*, 7903–792.
- Vernik, L. (1998), Acoustic velocity and porosity systematics in siliciclastics, *Log Anal.*, *39*(4), 27–35.
- Vrolijk, P., et al. (1998), Hydrostatic consolidation tests of undeformed, clay-rich samples from the Barbados accretionary prism, Leg 156, *Proc. Integr. Ocean Drill. Program, 171A*, 107–116, doi:10.2973/odp.proc.ir.2171a.2108.1998.
- Wetzel, A. (1986), Anisotropy and modes of deposition of pelitic Mississippi fan deposits, *Initial Rep. Deep Sea Drill. Proj.*, *96*, 811–818, doi:10.2973/dsdp.proc.2996.2152.1986.
- Wetzel, A. (1987), Sedimentological significance of strain and sonic velocity anisotropy in fine-grained turbiditic and hemipelagic deep-sea sediments—An example from the Mississippi fan, *Mar. Geol.*, *74*, 191–207, doi:10.1016/0025-3227(87)90050-8.
- Wilkens, R. H., et al. (1992), Evaluation and prediction of shear wave velocities in calcareous marine sediment and rocks, *J. Geophys. Res.*, *97*, 9297–9305.
- Wood, A. B. (1941), *A Textbook of Sound*, G. Bell, London.